nature communications

Article

https://doi.org/10.1038/s41467-024-51780-1

Aberrant mitochondrial DNA synthesis in macrophages exacerbates inflammation and atherosclerosis

Received: 22 September 2023

Accepted: 16 August 2024

Published online: 26 August 2024

Check for updates

Niranjana Natarajan[1,9], Jonathan Florentin[1,9], Ebin Johny[1], Hanxi Xiao[2,3,4,5], Scott Patrick O'Neil[1], Liqun Lei[1], Jixing Shen[1], Lee Ohayon[1], Aaron R. Johnson[1], Krithika Rao[1], Xiaoyun Li[1], Yanwu Zhao[1], Yingze Zhang[1], Sina Tavakoli[1], Sruti Shiva[1,6], Jishnu Das[2,3,4] & Partha Dutta[1,2,7,8]

There is a large body of evidence that cellular metabolism governs inflammation, and that inflammation contributes to the progression of atherosclerosis. However, whether mitochondrial DNA synthesis affects macrophage function and atherosclerosis pathology is not fully understood. Here we show, by transcriptomic analyzes of plaque macrophages, spatial single cell transcriptomics of atherosclerotic plaques, and functional experiments, that mitochondrial DNA (mtDNA) synthesis in atherosclerotic plaque macrophages are triggered by vascular cell adhesion molecule 1 (VCAM-1) under inflammatory conditions in both humans and mice. Mechanistically, VCAM-1 activates C/EBPα, which binds to the promoters of key mitochondrial biogenesis genes - *Cmpk2* and *Pgc1a*. Increased CMPK2 and PGC-1α expression triggers mtDNA synthesis, which activates STING-mediated inflammation. Consistently, atherosclerosis and inflammation are less severe in $Apoe^{-/-}$ mice lacking *Vcam1* in macrophages. Downregulation of macrophage-specific VCAM-1 in vivo leads to decreased expression of LYZ1 and FCOR, involved in STING signalling. Finally, VCAM-1 expression in human carotid plaque macrophages correlates with necrotic core area, mitochondrial volume, and oxidative damage to DNA. Collectively, our study highlights the importance of macrophage VCAM-1 in inflammation and atherogenesis pathology and proposes a self-acerbating pathway involving increased mtDNA synthesis.

Cellular metabolism regulates various cellular functions, including energy production, growth, and proliferation. Furthermore, non-canonical roles of metabolism, such as cell phenotypic switch[1], differentiation[2], cellular senescence[3], neurogenesis[4], efferocytosis[5], memory formation[6], cell migration[7], and tissue repair[8] have been recently reported. Various pathways of cellular metabolism, such as fatty acid synthesis[9–11] and oxidation[12], and mitochondrial respiration[13] control the functions of immune cells including $CD8^+$ T, T_H17, and

[1]Pittsburgh Heart, Lung, Blood, and Vascular Medicine Institute, Division of Cardiology, Department of Medicine, University of Pittsburgh School of Medicine, University of Pittsburgh Medical Center, Pittsburgh, PA 15213, USA. [2]Department of Immunology, University of Pittsburgh, Pittsburgh, PA, USA. [3]Center for Systems Immunology, University of Pittsburgh, Pittsburgh, PA, USA. [4]Department of Computational and Systems Biology, University of Pittsburgh, Pittsburgh, PA, USA. [5]Joint CMU-Pitt PhD program in Computational Biology, Pittsburgh, PA, USA. [6]University of Pittsburgh School of Medicine Department of Pharmacology & Chemical Biology, Pittsburgh, PA, USA. [7]Department of Bioengineering, Swanson School of Engineering, University of Pittsburgh, Pittsburgh, PA, USA. [8]Veterans Affairs Pittsburgh Healthcare System, Pittsburgh, PA, USA. [9]These authors contributed equally: Niranjana Natarajan, Jonathan Florentin. e-mail: duttapa@pitt.edu

regulatory T cells. Similarly, cellular metabolism also shapes macrophage phenotype and function[14]. For instance, ATP citrate lyase and fatty acid synthase, decisive enzymes during de novo fatty acid production, are crucial to macrophage-mediated inflammation by promoting histone acetylation[15–17] and atherosclerosis propagation[18]. Exposure to butyrate, a short-chain fatty acid, equip macrophages with enhanced anti-microbial properties[11]. Moreover, uptake of triglycerides by macrophages by the scavenger receptor CD36 in macrophages supplies fatty acids to these cells, which leads to an alternative activation[19]. Similarly, mitochondria, the powerhouse of the cell, regulate the functions of macrophages. The receptor for succinate, a TCA cycle metabolite, exerts anti-inflammatory reprogramming of macrophages in a mouse model of obesity[20]. Inhibition of mitochondrial fission decreases efferocytosis, a process of apoptotic cell clearance by macrophages, and exacerbates atherosclerosis[5]. Additionally, macrophage-specific mitochondrial complex deficiency resulted in inflammatory macrophages with poor efferocytosis capacity, resulting in defective cardiac healing after myocardial infarction[21]. A recent study demonstrated that mitochondrial function is highly correlated with the degree of severity in heart failure with preserved ejection fraction[22]. These studies demonstrate that metabolism molds macrophage function. In contrast to the well-known role of cellular metabolism in immunity, the contributions of mtDNA synthesis in shaping inflammation under disease conditions have not been explored.

Mitochondrial homeostasis is maintained by two opposing processes- mitochondrial biogenesis and mitophagy, by which cells remove damaged mitochondria. Mitochondrial biogenesis, the process by which cells increase mitochondrial numbers to fulfill their energy needs[23,24], is a multistep process. The first step of mitochondrial biogenesis is mtDNA transcription[25]. There are several genes, which orchestrate mtDNA synthesis, such as peroxisome proliferator-activated receptor γ coactivator 1 alpha (*PGC1A*), Cytidine/Uridine monophosphate kinase 2 (*CMPK2*), and DNA polymerase γ (*POLG*). *PGC1A* is a transcriptional coactivator that induces transcription of nuclear encoded mitochondrial genes[26]. PGC-1α interacts with nuclear respiratory factors NRF1 and NRF2, which regulate the expression of the electron transfer chain subunits encoded by the nuclear genome[27]. Finally, there is increased expression of TFAM, which is a mtDNA binding protein and essential for mitochondrial genome maintenance[28]. *CMPK2*, which is a rate-limiting enzyme for mtDNA synthesis, is critical for the production of cytidine triphosphate[29]. The catalytic subunit encoded by the *POLG* gene and auxiliary dimeric subunit encoded by the *POLG2* gene are crucial in mtDNA replication[30]. In the second step, mtDNA-encoded genes are translated into proteins with the help of several translation factors encoded by nuclear DNA. These factors include mitochondrial initiation factors 2 and 3 (mtIF2 and mtIF3), mitochondrial elongation factors Tu, Ts, and G1 (mtEFTu, mtEFTs, and mtEFG1), mitochondrial translational release factor 1-like (mtRF1L), and mitochondrial recycling factors 1 and 2 (mtRRF1 and mtRRF2). Aberrant mtDNA synthesis not only occurs in aging but also in many diseases including neurodegeneration and cancer[25]. mtDNA replication is an inital effect of the neurodegenerative process in neurons[31]. As such, modulating mtDNA synthesis is a potential therapeutic strategy in various neurodegenerative diseases including Alzheimer's disease and Parkinson's disease[32]. PGC-1α levels are increased in cancer invasion and metstasis, and 2-methoxyestradiol has been shown to reduce mtDNA synthesis in osteosarcoma cells[32]. Although mtDNA synthesis has been reported to be crucial in many diseases, whether this process affects plaque macrophage function and atherogenesis has not been explored. The present study shows that myeloid vascular cell adhesion molecule-1 (VCAM-1) augments the production of *CMPK2* and *PGC1A*, increasing mtDNA synthesis in atherosclerosis.

VCAM-1 in endothelial cells has been shown to facilitate monocyte migration into the intima. VCAM-1 expression is triggered by a variety of stimuli including pro-inflammatory cytokines, reactive oxygen species (ROS), oxidized low density lipoprotein (ox-LDL), and shear stress[33] and is highly expressed by activated endothelial cells. VCAM-1 binds to very late antigen-4 (VLA-4), an integrin. This interaction is required for firm adhesion of monocytes to the luminal surface of the endothelium and their subsequent entry to the vasculature[34]. Consistent with the literature[35–38], the current study shows that macrophages, particularly foam cells in atherosclerotic plaques of humans and mice, express VCAM-1 at high levels. Although the role of endothelial VCAM-1 in monocyte extravasation during atherogenesis has been widely studied, the function of macrophage VCAM-1 is less understood.

The goal of this study is to A) understand the role of aberrant mtDNA synthesis in macrophage-mediated inflammation and atherosclerosis, B) to examine myeloid VCAM-1-mediated regulation of mitochondrial metabolism, and C) to discern the role of myeloid VCAM-1 in atherogenesis. Here, we demonstrate increased VCAM-1 expression in human and mouse atherosclerotic plaque macrophages. Mice lacking *Vcam1* in macrophages exhibit reduced atherosclerotic plaque and necrotic core areas. *Vcam1* silencing in macrophages diminishes oxidized LDL-mediated inflammation, oxidative phosphorylation, and mtDNA synthesis in vitro. Selective silencing of mtDNA synthesis genes *Cmpk2*, *Pgc1a*, and *Polg* in macrophages in vivo causes a significant diminution in plaque burden and an increase in plaque stability in $Ldlr^{-/-}$ mice on atherogenic diet. Furthermore, we demonstrate that VCAM-1-mediated oxidized and fragmented DNA signals through the stimulator of interferon genes (STING) pathway to decrease the expression of *FCOR* and *LYZ1*, and augment inflammation. Our findings demonstrate the role of macrophage VCAM-1 in encouraging mtDNA synthesis to increase inflammation and aggravate atherosclerosis. Mitochondrial dynamics in immune cells play a key role in atherogenesis and cardiovascular disease. While increased mitochondrial DNA damage has been documented in CVD, our study establishes the pro-inflammatory effect of mtDNA in atherosclerotic macrophages and downstream signaling through the cGAS – STING pathway.

Results

Macrophage VCAM-1 expression is correlated with mitochondrial volume and DNA oxidative stress

VCAM-1 is an adhesion molecule, mainly expressed by endothelial cells, facilitating extravasation of leukocytes, especially monocytes, to the intima[39–41]. VCAM-1 is reported to be expressed by other cell types such as dendritic cells and macrophages[42,43]. However, little is known about the functions of VCAM-1 expressed by macrophages. Consitent with published reports[35–38], we observed that macrophages in human early (>20% blockade) and advanced (>70% blockade) carotid atherosclerotic plaques highly expressed VCAM-1 compared to healthy part (control) of the artery (Fig. 1A and B, H&E stained images of control, early, and advanced plaques are shown in Fig. S1A). The analyzes of published datasets confirmed increased VCAM-1 expression by atherosclerotic plaque macrophages (Fig. S1B). Single cell analysis of published data showed that various mouse and human macrophage subsets express high levels of Itga4 and Itgb1, which encode the VCAM-1 ligand VLA-4[44] (Fig. S1C, D, Cardiovascular atlas, https://pinto-lab.shinyapps.io/clara/). There were elevated levels of oxidative stress in atherosclerotic macrophages in advanced plaques as indicated by heightened presence of 8-hydroxy-2′ -deoxyguanosine (8-OHdG), a predominant form of oxidant-induced oxidative lesions in nuclear and mtDNA (Fig. 1A, B). Additionally, atherosclerotic macrophages in both early and advanced plaques had high expression of TOM20, a mitochondrial marker (Fig. 1A and B). Interestingly, we further noted that VCAM-1 expression in atherosclerotic macrophages was positively correlated with TOM20 and 8-OHdG staining (Fig. 1C). Moreover, necrotic core area was also positively correlated with macrophage VCAM-1, 8-OHdG, and TOM20 (Fig. 1D). We observed a parallel

https://doi.org/10.1038/s41467-024-51780-1

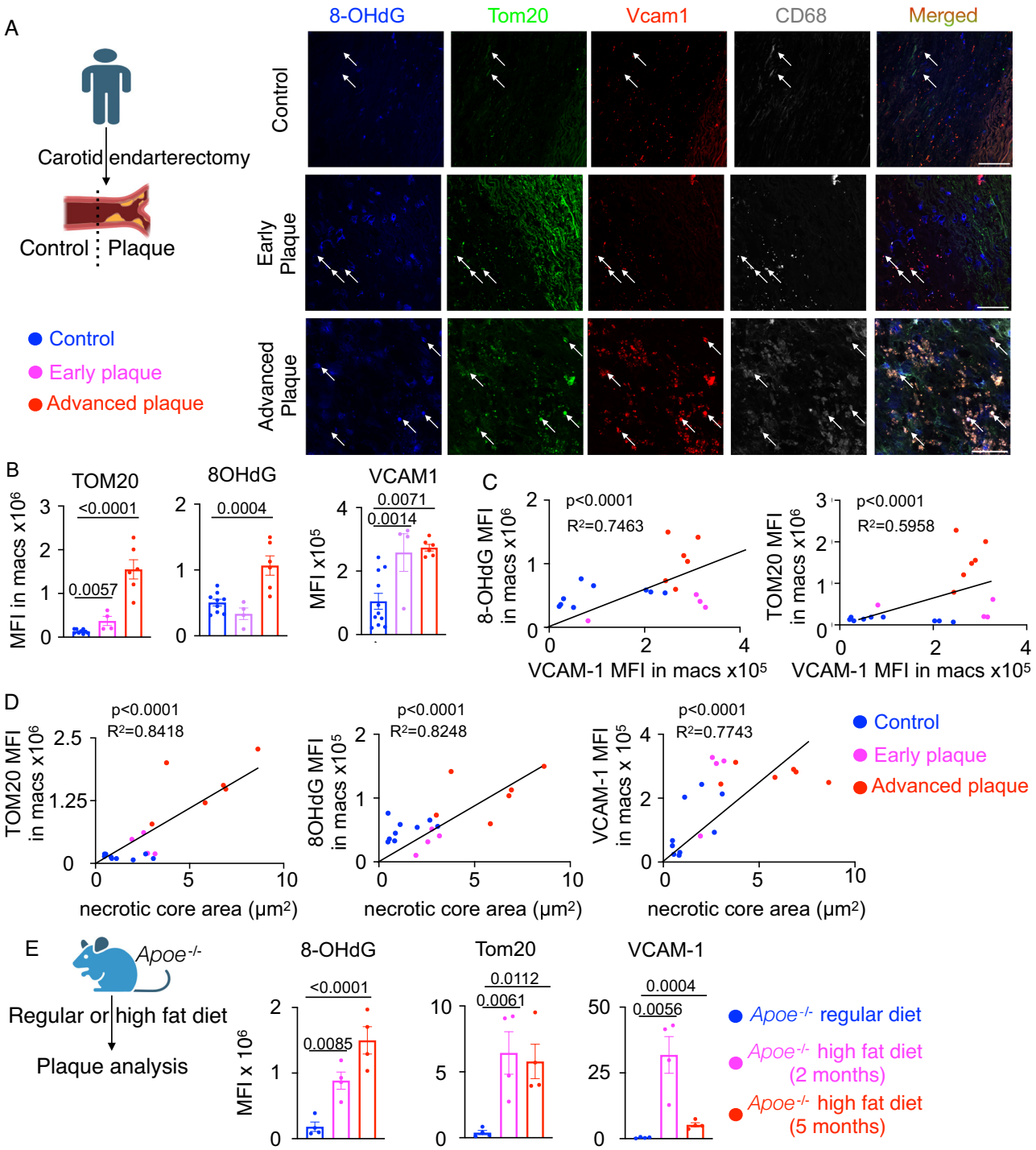

Fig. 1 | VCAM-1 is highly expressed in human and mouse plaque macrophages and correlates with increases in mitochondrial volume and oxidative DNA damage. A Tissue sections of early, and advanced plaque and control (healthy) human carotid arteries were stained with antibodies against 8OHdG (oxidative DNA damage), CD68 (macrophage), TOM20 (mitochondrial volume), and VCAM-1. scale bar= 50 μm. Representative images shown from 2 cohorts of carotid samples: 1. advanced plaque and control from endarterectomy at UPMC and 2. intermediate plaques from NDRI. **B** VCAM-1, 8OHdG, and TOM20 mean fluorescent intensities (MFI) in control and plaque macrophages in humans are measured, $n = 9$ (Control), 4 (early plaque), 6 (advanced plaque). Two-tailed t-test (Tom20), One-way ANOVA and post-hoc Fisher LSD test (8OHdG and VCAM-1). **C**, **D** Correlations among TOM20, 8-OHdG, and VCAM-1 MFI in macrophages (CD68$^+$), $n = 9$ (Control), 4 (early plaque), and 6 (advanced plaque) (**C**), and necrotic core area and 8-OHdG, TOM20, and VCAM-1 MFI in macrophages, $n = 9$ (Control), 4 (early plaque), 6 (advanced plaque) (**D**) in human carotid plaques have been shown. The data were pooled from two independent experiments. **E** MFI of CD68, VCAM-1, TOM20, and 8OHdG in aortic root macrophages of female *Apoe*$^{-/-}$ mice on regular and high fat diets for 2 and 5 months have been assessed by confocal microscopy. 8-OHdG: regular diet vs. 2 months HFD, 2 months HFD vs. 5 months HFD; TOM20 regular diet vs. 2 months HFD, regular diet vs. 5 months HFD; VCAM-1: regular diet vs. 2 months HFD one-way ANOVA and post-hoc Fisher LSD. VCAM-1, regular diet vs. 2 months HFD, 2-tailed t-test. ($n = 4$/group). Bar graphs in 1B, E shown as mean ± SEM.

increase in VCAM-1, TOM20 and 8-OHdG in mouse atherosclerotic macrophages in *Apoe*$^{-/-}$ mice fed with an atherogenic diet for 2 (early plaques) and 5 (advanced plaques) months (Figs. 1E and S1E). We observed that the atherogenic diet itself increased the levels of TOM20 and VCAM-1 but not 8-OHdG in aortic macrophages of C57BL/6 mice (Fig. S1F, G).

To characterize VCAM-1+ plaque macrophages, we carried out bulk RNA seq on sorted aortic VCAM-1^{+} and VCAM-1^{-} macrophages (Fig. S2A-S2B). This experiment revealed enrichment of the genes involved in the pathways, such as activation of macrophages, differentiation of macrophages, and stimulation of antigen presenting cells, in VCAM-1^{+} atherosclerostic macrophages (Fig. S2C). Furthermore, our analysis demonstrated that several upstream regulators, such as IL10RA, MAFB, and MAPKAPK2, which are crucial in atherogenesis[45–50], were upregulated in VCAM-1^{+} macrophages (Fig. S2D). Finallly, mtROS levels were significantly greater in VCAM-1^{+} macrophages compared to VCAM-1^{-} macrophages (Fig. S2E).

Macrophage VCAM-1 expression triggers inflammation and accelerates atherosclerosis

To explore the role of VCAM-1 expressed by macrophages in inflammation in atherosclerosis, we generated mice lacking *Vcam1* in macrophages on the *Apoe*$^{-/-}$ background (*Apoe*$^{-/-}$ *LyzM*$^{Cre/+}$ *Vcam1*$^{fl/fl}$) and fed these mice with an atherogenic diet. Among the myeloid cells, macrophages and monocytes in the wildtype mice had detectable VCAM-1 expression while only macrophages of *Apoe*$^{-/-}$ *LyzM*$^{Cre/+}$ *Vcam1*$^{fl/fl}$ mice exhibited reduction in VCAM-1 levels (Figs. S3A-S3B). We further validated the efficiency of *Vcam1* deletion in aortic macrophages and bone marrow-derived macrophages (BMDM) in *LyzM*$^{Cre/+}$ *Vcam1*$^{fl/fl}$ mice (Fig. S3C-S3E). *Apoe*$^{-/-}$ *LyzM*$^{Cre/+}$ *Vcam1*$^{fl/fl}$ mice had less atherosclerotic burden as shown by the decreased plaque and necrotic core areas compared to *Apoe*$^{-/-}$ *LyzM*$^{+/+}$ *Vcam1*$^{fl/fl}$ littermate control mice (Fig. 2A, Figure S3F-S3H). However, the serum cholesterol levels were unchanged when these mice were fed with a regular or atherogenic diet (Fig. 2B). Additionally, *Apoe*$^{-/-}$ *LyzM*$^{Cre/+}$ *Vcam1*$^{fl/fl}$ mice had suppressed systemic inflammation as shown by the lower levels of serum IL-5, IL-17, GM-CSF, and TNF-α when fed with a hight fat diet (Fig. 2C) and suppressed serum concentration of G-CSF on a regular diet (Fig. S3I). Interestingly, mice with myeloid *Vcam1* deficiency and fed with a regular diet exhibited higher levels of eotaxin and RANTES (Fig. S3I). To discern whether macrophages lacking *Vcam1* secrete less inflammatory cytokines, we cultured BMDM from *LyzM*$^{Cre/+}$ *Vcam1*$^{fl/fl}$ and *LyzM*$^{+/+}$ *Vcam1*$^{fl/fl}$ mice. Upon exposure to oxidized LDL, BMDM lacking *Vcam1* secreted diminished amounts of pro-inflammatory cytokines and chemokines such as IL-1α, IL-1β, IL-12, IL-17A, TNF-α, and MCP-1 (Fig. 2D). Interestingly, the levels of Th2 cytokines, such as IL-4 and IL-5, also decreased in the culture of *Vcam1*-deficient macrophages. In line with this, eosinophil frequencies and numbers decreased, and the amount of plaque malondialdehyde, an oxidation specific epitope, was lower in myeloid *Vcam1*-deficient mice (Fig. S3J–L). However, Th2 frequencies and numbers increased in myeloid *Vcam1*-deficient mice (Fig. S3J, K). *Il6* and *Ifnb* mRNA expression was significantly lower in *Vcam1*$^{-/-}$ BMDM (Fig. 2E). In line with the positive correlations of VCAM-1 with 8-OHdG and TOM20, we observed significant reduction in the expression of the DNA damage and mitochondrial markers in *Vcam-1*$^{-/-}$ plaque macrophages (Figs. S4A, B). However, 8-OHdG and TOM20 expression in macrophages was not significantly correlated with CCR2 levels (Fig. S4C, D) suggesting that the correlations among VCAM-1, 8-OHdG, and TOM20 are not due to increased accumulation of macrophages. The absence of *Vcam1* in these mice did not affect the numbers of leukocyte subsets in the aorta, spleen, bone marrow, and blood (Figs. S4E-S4G and S5A). Since endothelial VCAM-1 facilitates adhesion of macrophages in atherosclerotic plaques[36], we explored the possibility that macrophage VCAM-1 promotes migration of these myeloid cells in atherosclerotic plaques. We found that oxidized LDL increased the expression of the retention factors, such as *Ccr7*, *Ntr1*, Cd146 and *Sema3* in *Vcam1*$^{+/+}$ macrophages (Fig. S5B). In contrast, the levels of these genes were unaltered in *Vcam1*$^{-/-}$ macrophages upon oxidized LDL treatment compared to the native LDL-treated *Vcam1*$^{-/-}$ macrophages. However, *Vcam1* deficiency did not significantly change the migration of macrophages towards an Mcp-1 gradient in vitro (Fig. S5C).

To better characterize the macrophage subsets and transcriptional changes in *Ldlr*$^{-/-}$ *LysM*$^{+/+}$ *Vcam1*$^{fl/fl}$ and *Ldlr*$^{-/-}$ *LysM*$^{cre/+}$ *Vcam1*$^{fl/fl}$ mice, we performed spatial single cell transcriptomics in the aortic roots of these mice. (Figs. 2F, G and S6). An overview of spatial transcriptomics analyzes workflow is shown in Fig. S6A. A standard preprocessing pipeline (Methods) was followed by cell type deconvolution, using Robust Cell Type Deconvolution (RCTD), to identify macrophage niches. A murine single-cell RNA-seq reference dataset from aortic tissue served as the basis for cell type deconvolution[44]. The representative spatial data show distribution of cells such as macrophages, smooth muscle cells, and fibroblasts (Fig. 2F). We then performed differential expression analyzes both overall and within individual macrophage clusters corresponding to different spatial niches. Aortic macrophages in *Ldlr*$^{-/-}$ *LysM*$^{+/+}$ *Vcam1*$^{fl/fl}$ mice expressed higher levels of *mt-Nd5* and *Tspo*, critical in mitochondrial metabolism, compared to the ones in *Ldlr*$^{-/-}$ *LysM*$^{Cre/+}$ *Vcam1*$^{fl/fl}$ mice (Fig. 2G). The dimensionality reduction analyzes of the spatial transcriptomics data unveiled four clusters of macrophages in the aortic roots (Clusters 0, 2, 5, and 12) (Fig. S6B, C). The Clusters 0 and 2 expressed most differential genes (Fig. S6C). We also identified the pathways downregulated in *Ldlr*$^{-/-}$ *LysM*$^{cre/+}$ *Vcam1*$^{fl/fl}$ aortic macrophages (Fig. S6D). To gain more systematic insights into corresponding pathways, over-representation analyzes were conducted, both overall and within the different macrophage clusters. While canonical marker genes for these clusters have similar expression levels, they correspond to different spatial microniches based on their proximity to other cell types. Across these clusters, we observed that the pathways, such as immune system, neutrophil degranulation, adaptive immune system, and antigen processing and cross presentation, were suppressed in aortic macrophages in the absence of *Vcam1*. Our results suggest that the transcriptional and phenotypic alterations that we see in the absence of *Vcam1* transcend macrophage subsets.

Macrophage VCAM-1 augments mitochondrial metabolism

Various studies have reported that atherosclerosis is linked with mitochondrial dysfunction and increased mitochondrial ROS generation[51–54]. Mitochondrial ROS are produced by enhanced mitochondrial respiration[55,56]. Knowing that macrophage metabolism plays a substantial role in the outcome of atherosclerosis[57] and VCAM-1 expression is correlated with TOM20 levels (Fig. 1), we investigated whether VCAM-1 expression in atherosclerotic macrophages modulates their mitochondrial metabolism. Seahorse experiments revealed that *LyzM*$^{+/+}$ *Vcam1*$^{fl/fl}$ macrophages treated with oxidized LDL had higher oxygen consumption rate (OCR) as demonstrated by higher basal and maximal respiration and spare capacity, compared to the native LDL-treated group (Fig. 3A and Table S1). In contrast, we did not observe a similar increase in OCR of *Vcam1*-deficient (*LyzM*$^{cre/+}$ *Vcam1*$^{fl/fl}$) macrophages after oxidized LDL treatment. Similarly, while *LyzM*$^{+/+}$ *Vcam1*$^{fl/fl}$ macrophages treated with oxidized LDL had higher mitochondrial volume and membrane potential, *LyzM*$^{cre/+}$ *Vcam1*$^{fl/fl}$ macrophages did not exhibit increases in these parameters upon oxidized LDL exposure (Figs. 3B and S7A). Similarly, while there was no difference in basal glycolysis, we found diminished maximal and glucose-dependent (2-DG-sensitive) maximal glycolysis in *Vcam1*-deficient macrophages treated with oxLDL compared to *Vcam1*$^{+/+}$ macrophages (Fig. S7B–E). Consistently, *Vcam1*$^{-/-}$ macrophages had reduced amount of lactate (Fig. S7F). We next examined mitochondrial complex activity and expression. Mitochondrial complexes III and IV

https://doi.org/10.1038/s41467-024-51780-1

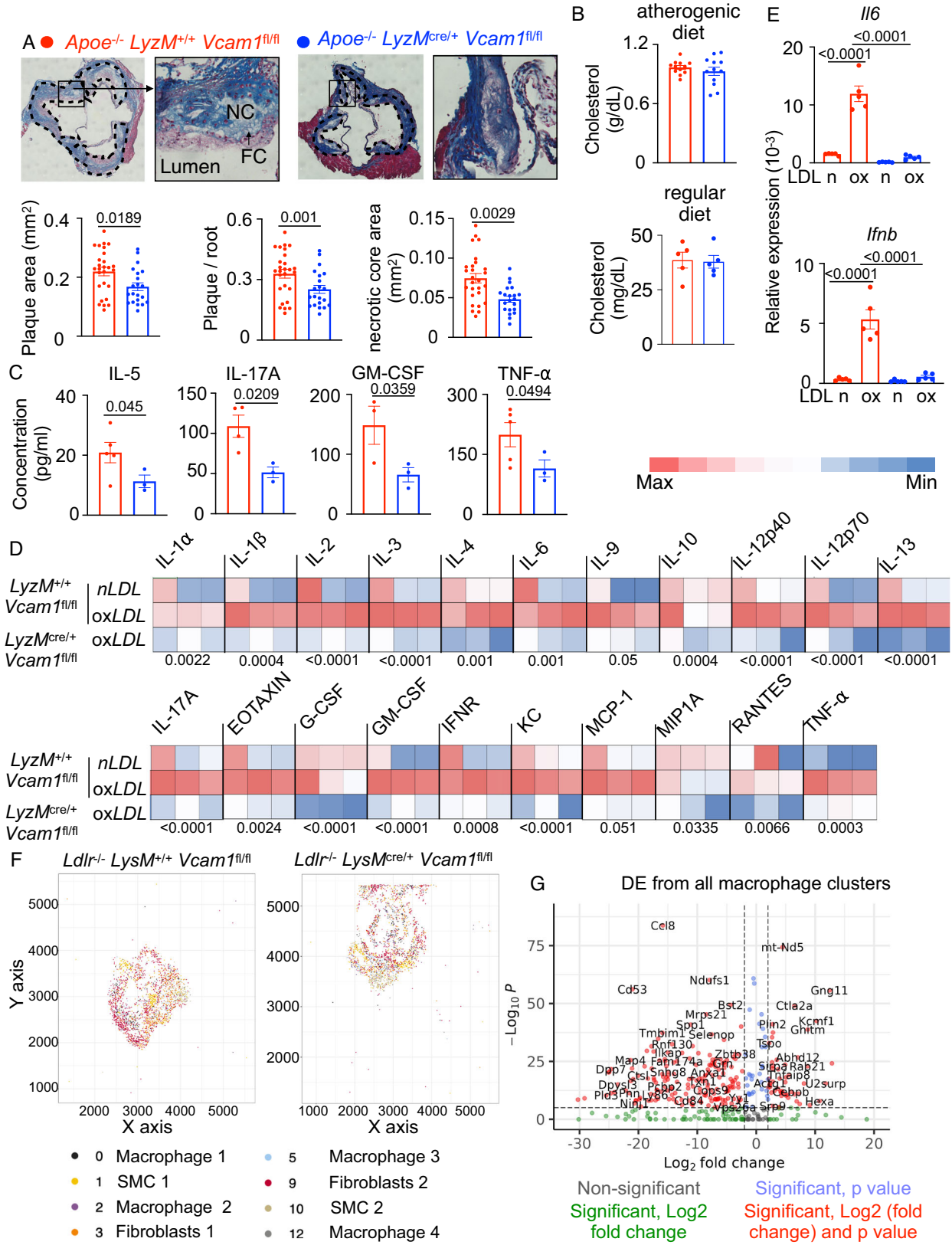

activities were diminished in macrophages lacking *Vcam1* (Fig. 3C). In addition, the expression of complexes II and III was reduced in these macrophages (Fig. 3D and E). Finally, to understand whether *Vcam1* deficiency impairs the progression of the tricarboxylic acid (TCA) cycle, we performed a targeted metabolomics experiment to measure the TCA metabolites in *LysM*$^{+/+}$ *Vcam1*$^{fl/fl}$ and *LysM*$^{Cre/+}$ *Vcam1*$^{fl/fl}$ BMDM in presence of either native or oxidized LDL. Oxidized LDL exposure decreased the amount of most TCA metabolites in the culture of *LysM*$^{+/+}$ *Vcam1*$^{fl/fl}$ macrophages compared to *LysM*$^{cre/+}$ *Vcam1*$^{fl/fl}$ macrophages, indicating accelerated usage of the the TCA cycle metabolites in the wildtype macrophages (Fig. S7G). Consistently, using a ^{13}C glucose labeling experiment, which informs about the

Fig. 2 | Macrophage VCAM-1 promotes atherogenesis. A Representative images of Masson's trichrome-stained aortic root sections from *Apoe*$^{-/-}$ *LyzM*$^{+/+}$ *Vcam1*$^{fl/fl}$ and *Apoe*$^{-/-}$ *LyzM*$^{cre/+}$ *Vcam1*$^{fl/fl}$ mice are provided. Plaque area, plaque/root ratio, and necrotic core area have been calculated ($n = 9$ *LyzM*$^{cre/+}$ *Vcam1*$^{fl/fl}$, 7 *LyzM*$^{+/+}$ *Vcam1*$^{fl/fl}$, all female mice used). The data were pooled from two independent experiments. Each data point represents one plaque in the aortic root, two-tailed t-test used. **B** Serum cholesterol levels of *Apoe*$^{-/-}$ *LyzM*$^{+/+}$ *Vcam1*$^{fl/fl}$ and *Apoe*$^{-/-}$ *LyzM*$^{cre/+}$ *Vcam1*$^{fl/fl}$ female mice on atherogenic diet (top panel, $n = 12$/group) and *LyzM*$^{+/+}$ *Vcam1*$^{fl/fl}$ and *LyzM*$^{cre/+}$ *Vcam1*$^{fl/fl}$ mice on regular diet (bottom panel, $n = 5$/group) were quantified by an enzymatic assay, two-tailed t-test used. **C** IL-5, IL-17A, GM-CSF, and TNF-α concentrations by Luminex were measured ($n = 4$,5 *Vcam1*$^{+/+}$, $n = 3$ *Vcam1*$^{-/-}$), one-tailed t-test used. **D** Luminex assay was used to quantify the inflammatory biomarkers in the cell culture supernatants of female *LyzM*$^{+/+}$ *Vcam1*$^{fl/fl}$ and *LyzM*$^{cre/+}$ *Vcam1*$^{fl/fl}$ BMDM treated with oxidized LDL ($n = 3$/group, one-tailed t-test p values comparing oxLDL treated *LyzM*$^{+/+}$ *Vcam1*$^{fl/fl}$ and *LyzM*$^{cre/+}$ *Vcam1*$^{fl/fl}$ BMDM shown). **E** Expression of *Il6* and *Ifnβ* in BMDM obtained from *Apoe*$^{-/-}$ *LyzM*$^{+/+}$ *Vcam1*$^{fl/fl}$ and *Apoe*$^{-/-}$ *LyzM*$^{cre/+}$ *Vcam1*$^{fl/fl}$ mice was assessed ($n = 5$/group, one-way ANOVA with post-hoc Fisher LSD test). **F** Representative spatial distribution of various cell types in the aortic roots from single-cell spatial transcriptomics analysis of *Ldlr*$^{-/-}$ *LysM*$^{+/+}$ *Vcam1*$^{fl/fl}$ and *Ldlr*$^{-/-}$ *LysM*$^{cre/+}$ *Vcam1*$^{fl/fl}$ mice. **G** The volcano plot of differential gene expression in aortic macrophages of *Ldlr*$^{-/-}$ *LysM*$^{+/+}$ *Vcam1*$^{fl/fl}$ and *Ldlr*$^{-/-}$ *LysM*$^{cre/+}$ *Vcam1*$^{fl/fl}$ mice, data plotted as $\log_2$(fold change) vs. $\log_{10}$(FDR corrected P-value). $n = 3$/group. Bar graphs in 2A-C, E shown as mean ± SEM.

incorporation of carbon derived from the labeled glucose into new metabolites, we observed elevated ^{13}C-labeled TCA metabolites in *LyzM*$^{+/+}$ *Vcam1*$^{fl/fl}$ macrophages (Fig. 3F and Table S2-S10). This finding suggests an accelerated usage of the metabolites in the TCA cycle in these macrophages. Taken together, these data suggest that macrophage VCAM-1 increases mitochondrial metabolism.

VCAM-1 enhances mtDNA synthesis to unleash inflammation

We observed that macrophages in atheromas of patients and mice have elevated VCAM-1 and TOM20 mean fluorescence intensity (Fig. 1). Additionally, because VCAM-1 deficiency limits oxidized LDL-mediated expansion of mitochondrial volume (Fig. 3B), we hypothesized that VCAM-1 amplifies mtDNA synthesis under pro-inflammatory conditions. We measured *D-loop/Tert* ratios to quantify mtDNA. Oxidized LDL treatment triggered mtDNA synthesis and increased cytoplasmic mtDNA in *Vcam1*$^{+/+}$ BMDM while *Vcam1* deficiency abrogated this response (Fig. 4A and Fig. S8A). Mitochondrial volume is also regulated by mitophagy[58], a process by which aged and damaged mitochondria are removed. Mitophagy was assessed by various strategies- transgenic mice expressing mt-Keima, which is a pH-dependent fluorescent protein, and immunoblot to assess Parkin, which is essential for ubiquitination and clearance of mitochondrial proteins[59] (Fig. S8B–D). We observed that VCAM-1 was dispensable for mitophagy. mtDNA synthesis relies upon the genes including *Cmpk2, Pgc1a*, *Polg*, *Diacylglycerol kinase* (*Dgk*), and *Adenylate kinase 2* (*Ak2*)[27,30,60]. In line with raised mtDNA synthesis in response to oxidized LDL, the expression of these genes was heightened in *Vcam1*$^{+/+}$ BMDM (Fig. 4B). However, the absence of *Vcam1* dampened the expression of the genes. We also observed complementary alterations in EdU incorporation and 8-OHdG in mitochondria (Figs. 4C, D, and S9A). Since we observed that *Vcam1* deficiency decreased mtDNA synthesis and inflammation, we ascertained the role of reduced mtDNA synthesis in dampening inflammation in *Vcam1*$^{-/-}$ macrophages. Both mitochondrial and nuclear DNA transfection augmented the expression of the genes encoding pro-inflammatory cytokines in *Vcam1*$^{-/-}$ BMDM (Fig. S9B) while mtDNA depletion in BMDM significantly curtailed oxLDL-mediated inflammation (Fig. S9C). To examine if mtDNA synthesis triggers inflammation in macrophages, we silenced *Polg* and *Cmpk2* expression in *Vcam1*$^{+/+}$ BMDM exposed to native or oxidized LDL. As expected siControl-treated BMDM responded to oxidized LDL treatment by increasing the expression of *Ifnb*, *Il1b*, *Il6*, and *Tnfa* while si*Polg* abrogated the inflammatory response to oxLDL (Fig. 4E). Similarly, si*Cmpk2* treatment abolished oxidized LDL-induced exaggerated production of IL-6 and TNF-α at both mRNA (Fig. 4F) and protein (Fig. S9D) levels. Conversely, *CMPK2* overexpression increased *IL1B*, *IL6*, and *TNFA* expression in THP-1 macrophages treated with either siControl or si*VCAM1* (Fig. 4G, Fig. S9E). As expected, *Cmpk2* silencing decreased D-loop/Tert ratio in BMDM treated with oxidized LDL (Figs. S9F). Mitochondrial ROS is one of the main causes of mtDNA damage and may induce leakage of mtDNA into the cytosol[61]. In line with this report, *Vcam1*$^{-/-}$ BMDM had significantly suppressed levels of mitochondrial ROS, and inhibition of mitochondrial ROS in *Vcam1*$^{+/+}$ BMDM led to suppressed inflammatory gene expression (Figs. S9G, H). Damaged mtDNA can bind to cGAS. The binding of mtDNA to cGAS activates the production of a second messenger, cGAMP, which in turn activates the adaptor STING[62]. We found that oxLDL treatment significantly increased the expression of STING in macrophages (Fig. S10A). The other mtDNA sensors were not significantly altered. Consistently, we observed that the ratio of pSTING/STING was significantly suppressed in absence of *Vcam1* (Fig. S10B). Moreover, *Cmpk2* and *Pgc1a* but not *Polg* silencing decreased p-Sting/Sting ratios (Fig. S10C–S10D). To further ascertain the role of STING in VCAM-1-mediated inflammation, we used loss and gain of function strategies. We found that the expression of the pro-inflammatory cytokines in response to oxidized LDL was depressed in BMDM after *Sting* knock down (Figs. 4F and S10E). STING overexpression in THP-1 macrophages magnified oxidized LDL-induced inflammatory cytokine expression (Fig. 4G). Validation of *Polg*, *Cmpk2*, *Sting*, and *Vcam1* silencing, and *Cmpk2* overexpression is shown in Figure S10E. In sum, these data suggest that macrophage VCAM-1 augments mtDNA synthesis in the presence of an inflammatory stimulus and escalates inflammation via the STING pathway.

mtDNA synthesis genes in macrophages augments atherosclerosis

Since our data indicate that macrophage VCAM-1 exacerbates inflammation via upregulation of mtDNA synthesis, we tested the role of three major mtDNA synthesis genes in atherosclerosis, *Polg, Ppargc1a* (*Pgc1a*), and *Cmpk2*. Using a macrophage-specific in vivo siRNA delivery approach as we reported previously[63], we observed that silencing of these genes in Ldlr-/- mice fed with an atherogenic diet led to significant decreases in plaque size and necrotic core area relative to the control group while the fibrous cap thickness increased (Fig. 4H, I). However, we did not observe significant changes in the abundance of leukocyte populations in the aortas or differences in mitochondrial membrane potential or volume (Fig. S11A-S11E). Interestingly, we observed modest elevation in splenic B cell numbers after *Polg* and *Pgc1a* silencing, and bone marrow T cells after *Cmpk2*, *Polg*, and *Pgc1a* knockdown compared to the control siRNA group (Fig. S11B, C). Macrophages in atherosclerotic plaques of mice treated with siRNA against the mtDNA synthesis genes (incorporated in DOTAP nanoparticles that are preferentially engulfed by macrophages) significantly reduced the expression of TOM20 and 8-OHdG in atherosclerotic plaque macrophages (Fig. S12A, B). To understand if these genes alter macrophage phenotype, we stained aortic roots sections with antibodies against iNos and found that iNos expression was significantly decreased in atherosclerotic plaque macrophages after the silencing of the mitochondrial biogenesis genes. Furthermore, among the three mitochondrial biogenesis genes we tested, *Cmpk2* silencing in macrophages in mice with atherosclerosis resulted in the highest numbers of differentially expressed genes. These genes, such as *Gdf15, Ndufa5, Ndufv2, Ndufb3, Atp6v1e1, Map3k6, Lrp8, Ifnlr1, Acly, Gpr82, Ccl6,8,9*, and *Ncoa4*, are critical in inflammation, atherosclerosis, and cellular metabolism (Fig. S12C)[18,64–66].

https://doi.org/10.1038/s41467-024-51780-1

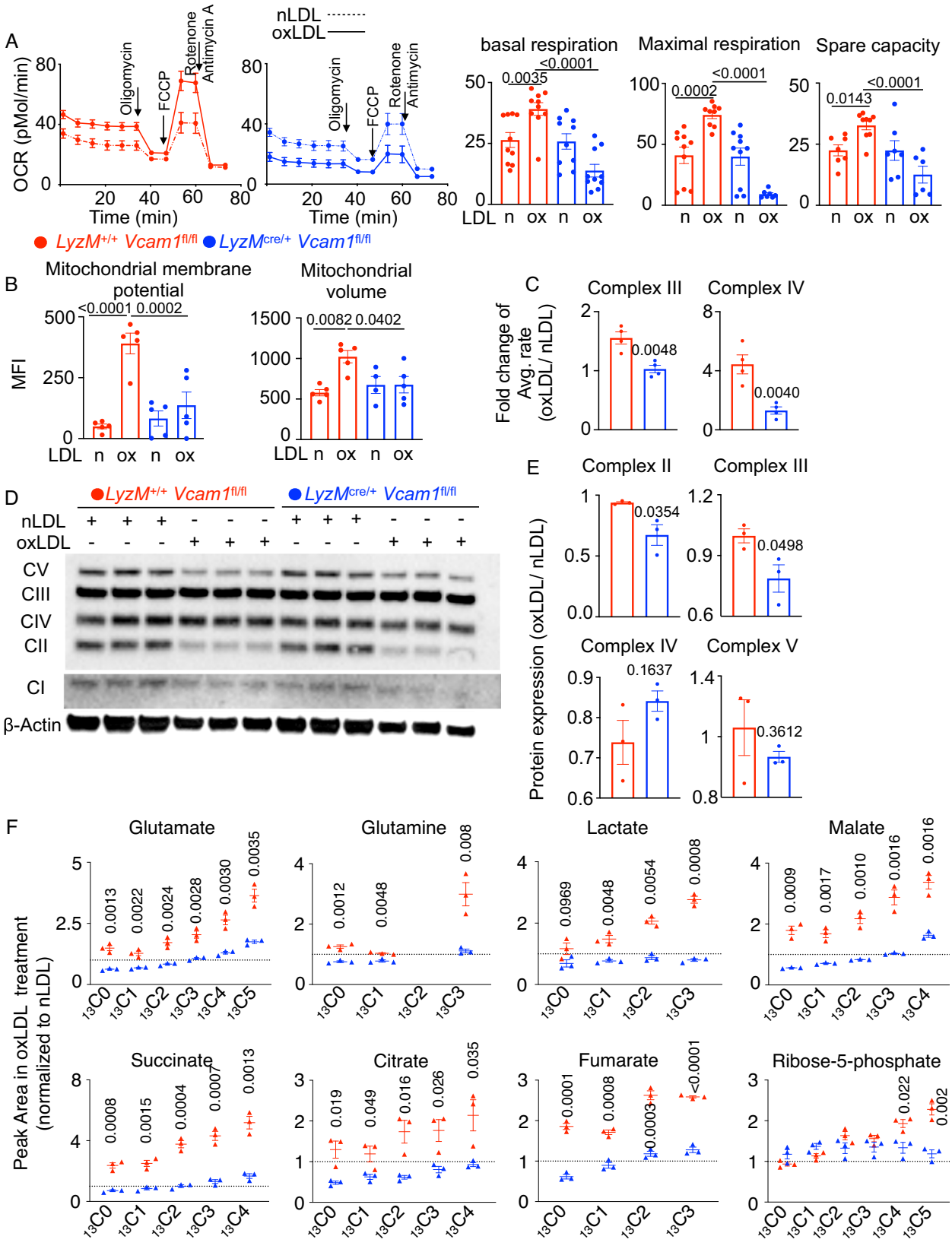

VCAM-1 modulates the downstream genes to enhance inflammation

To further delineate the molecular mechanisms by which VCAM-1 exacerbates atherosclerosis, we generated bone marrow chimeric mice by transplanting *LyzM*$^{+/+}$ *Vcam1*$^{fl/fl}$ and *LyzM*$^{cre/+}$ *Vcam1*$^{fl/fl}$ bone marrow cells in *Ldlr*$^{-/-}$ mice and fed them with an atherogenic diet for four months. RNA sequencing was performed on sorted aortic macrophages from these mice. We found that 25 genes were differentially expressed in plaque macrophages lacking *Vcam1* (Figs. 5A and S13A). Among these genes, the expression of *Fcor, Nid1, Wisp2, Zfp300, Zfp940, Cxcr6, Nid1, Apoc4*, and *Itgb7* were stable across the samples and their differential expression between the groups was validated by

Fig. 3 | Macrophage VCAM-1 upregulates mitochondrial metabolism. **A** Seahorse experiments were performed to measure oxygen consumption rates (OCR), basal respiration, maximal respiration, and spare capacity in BMDM from *LyzM*$^{+/+}$ *Vcam1*$^{fl/fl}$ and *LyzM*$^{cre/+}$ *Vcam1*$^{fl/fl}$ treated with either native (n) or oxidized (ox) LDL ($n = 10$/group). The data were pooled from two independent experiments. One-way ANOVA with post-hoc Fisher LSD test was used. **B** Mitochondrial membrane potential and mitochondrial volume were calculated by mitotracker green and deep red staining, respectively, by flow cytometry ($n = 5$/group). One-way ANOVA with post-hoc Fisher LSD test was used. **C**–**E** Mitochondrial complex activities by enzymatic assays (**C**) and mitochondrial complex levels by immunoblot (**D** and **E**, normalized to β actin) were evaluated ($n = 3$/group, two-tailed t-test used). **F** ^{13}C glucose flux analyzes of the Krebs cycle metabolites by mass spectrometry were determined in *LyzM*$^{+/+}$ *Vcam1*$^{fl/fl}$ and *LyzM*$^{cre/+}$ *Vcam1*$^{fl/fl}$ BMDM ($n = 3$/group). The values in oxLDL-treated BMDM were normalized to those after nLDL treatment. All bar graphs shown as mean ± SEM.

qPCR (S13A**, right panel**). We observed that the expression of *Fcor, Lyz1, Nid1, Wisp2, Zfp300*, and *Zfp940*, referred to as the VCAM-1 downstream genes hereafter, was heightened in *Vcam1*-deficient macrophages, suggesting their roles in suppressing inflammation. Indeed, silencing these genes in BMDM significantly increased overall inflammation (Fig. 5B). Because we found that VCAM-1-induced inflammation is dependent on the mtDNA synthesis genes (Fig. 4), we hypothesized that the VCAM-1 downstream genes are also controlled by the mtDNA synthesis genes. In line with this, we observed that *Cmpk2* (Fig. 5C) and *Polg* (Fig. 5D) silencing upregulated the VCAM-1 downstream genes in BMDM in presence of oxidized LDL. We also overexpressed *CMPK2* and *STING* in THP-1 macrophages to examine their effects on the VCAM-1 downstream genes in presence or absence of si*VCAM1* (Fig. 5E). As expected, *VCAM1* silencing increased the expression of the VCAM-1 downstream genes compared to the control. However, *CMPK2* and *STING* overexpression rescinded the upregulation of the VCAM-1 downstream genes after *VCAM1* silencing (Figs. 5E and S13B). These data suggest that the VCAM-1 downstream genes are regulated by *CMPK2* and *STING*. Finally, we observed that mtDNA transfection in BMDM lessened the expression of the VCAM-1 downstream genes (Fig. 5F). Cumulatively, these data suggest that VCAM-1 dampens the expression of downstream genes via mtDNA synthesis and the STING pathway, and the VCAM-1 downstream genes curb inflammation. To understand how VCAM-1 regulates Cmpk2, we compared the transcriptomic profiles of *Vcam1*$^{+/+}$ and *Vcam1*$^{-/-}$ plaque macrophages and observed that *CEBP/α* is a transcription factor regulated by VCAM-1 (Fig. S13C). We observed that the expression of this transcription factor was downregulated in BMDM lacking *Vcam1* (Figs. S13D). Ligand cross-linking of endothelial VCAM-1 activates calcium fluxes and Rac1[67]. In line with this report, we observed significantly reduced *Rac1* expression in response to oxLDL in *Vcam1*-deificient macrophages (Fig. S13E). Additionally, we saw a significant reduction in *Cebpα* levels after *Rac1* silencing in BMDM (Fig. S13F). Our in silico analysis has revealed that *CEBP/α* has a binding motif on the promoter regions of *Cmpk2, Pgc1a*, and *Polg* (Fig. S13C**, bottom panel**). The binding of *CEBP/α* to *Cmpk2* and *Pgc1a* but not *Polg* was reduced in absence of *Vcam1* (Fig. S13G). Consistently, *Cebpα* silencing significantly dampened the expression of *Cmpk2* and *Pgc1a* but not *Polg* in BMDM (Fig. S13H). Altogether, these data suggest that macrophage VCAM-1 increases the expression of *Cebpα*, which binds to the promoter regions of *Cmpk2* and *Pgc1a*, elevating their expression.

VCAM-1 exacerbates atherosclerosis by suppressing Fcor and Lyz1

We observed that, among the VCAM-1 downstream genes, the expression of *Fcor*, *Lyz1*, and *Wisp2* was detectable in atherosclerotic plaque macrophages and their expression was downregulated in aortic macrophages present in atherosclerotic lesions (Fig. 6A). To understand if these genes are critical for reduced atherogenesis in mice lacking *Vcam1* (Fig. 2), we generated bone marrow chimeric *Ldlr*$^{-/-}$ mice lacking *Vcam1* in macrophages (Fig. 6B). We silenced *Fcor*, *Lyz1*, and *Wisp2* in macrophages in these mice using siRNA incorporated in DOTAP nanoparticles (Fig. 6C). *Fcor* and *Lyz1*, but not *Wisp2*, silencing resulted in larger atherosclerotic plaques without changing fibrous cap thickness compared to control siRNA treated mice (Fig. 6D). Additionally, only si*Fcor* significantly increased necrotic core areas in atheromas. Interestingly, *Wisp2* knockdown in macrophages thickened fibrous caps without changing plaque and necrotic core areas. However, silencing of these genes did not significantly alter the numbers and frequencies of leukocytes in the aorta, blood, bone marrow, and spleen (Fig. S14A) and HDL, LDL+vLDL, and total cholesterol levels (Fig. S14B). Interestingly, *Lyz1* silencing, which did not change atherosclerotic plaque burden, exhibited non-significant reduction in HDL, LDL+vLDL, and cholesterol levels. Congruent with the atheroprotective roles of *Fcor* and *Lyz1* but not *Wisp2*, myeloid *STING* deficiency rose *Fcor* and *Lyz1*, but not *Wisp2*, expression in atherosclerotic plaque macrophages (Fig. S15A). RNA sequencing analyzes of aortic macrophages obtained from si*Fcor* and si*Lyz1*-treated mice showed upregulation of *Akt2, Chkb*, and *Fkbp5*, and downregulation of *Mmp14, Rrp9* and *Arg1* in both groups compared to siControl (Figs. 6E, S15B, and S15C). These genes have been implicated in atherogenesis, inflammation, and macrophage function[68–73]. Altogether, these data indicate that atherogenesis due to macrophage VCAM-1 is mediated by low *Fcor* and *Lyz1* expression (Fig. 6F).

Discussion

Atherosclerosis is the dominant cause of cardiovascular disease including myocardial infarction, stroke, and peripheral artery disease. Inflammatory macrophages are the most prevalent leukocytes within plaques. This cell population rises by differentiation of circulating inflammatory monocytes[74] and local proliferation of plaque resident macrophages[75]. In humans, the number of monocytes in the intima expands at a very young age and the development of plaque in young adults is not uncommon[76]. During atherogenesis, macrophages in a developing plaque take up lipoproteins and differentiate into foam cells. The plaque's microenvironment, such as cholesterol, hypoxia, and apoptotic cellular debris, orchestrates metabolic rewiring of foam cells[77,78]. Yet, if atherosclerosis propagates mtDNA synthesis in plaque macrophages and how this process affects inflammation and atherogenesis are not known. We observed that atherosclerotic plaque macrophages have VCAM-1-mediated high mtDNA synthesis, which amplifies inflammation and accelerates atherosclerosis progression.

VCAM-1 and its ligand VLA-4 have been shown to facilitate leukocyte, especially monocyte, entry into the intima. Although endothelial cells express VCAM-1 at high levels, hematopoietic cells, including monocytes, tissue macrophages, and dendritic cells, express this adhesion molecule in inflammatory conditions[42,43]. However, the functions of leukocyte VCAM-1 are understudied[79]. Many studies revealed the deleterious role of endothelial VCAM-1 in atherosclerosis[80–82]. However, the role of VCAM-1 expressed by atherosclerotic plaque macrophages and how the adhesion molecule regulates mitochondrial metabolism have not been investigated.

mtDNA synthesis can shape immunity[83,84]. Congruent with our findings in plaque macrophages, aortic samples from atherosclerotic patients had greater mtDNA oxidative damage than nonatherosclerotic aortic samples from age-matched transplant donors[85]. Interestingly, multiple studies showed that mtDNA drives noncanonical inflammation via the cyclic cGAS-STING signaling pathway in various diseases leading to the production of interferon-stimulated genes and inflammatory cytokines[86–89]. The binding of double-stranded DNA

https://doi.org/10.1038/s41467-024-51780-1

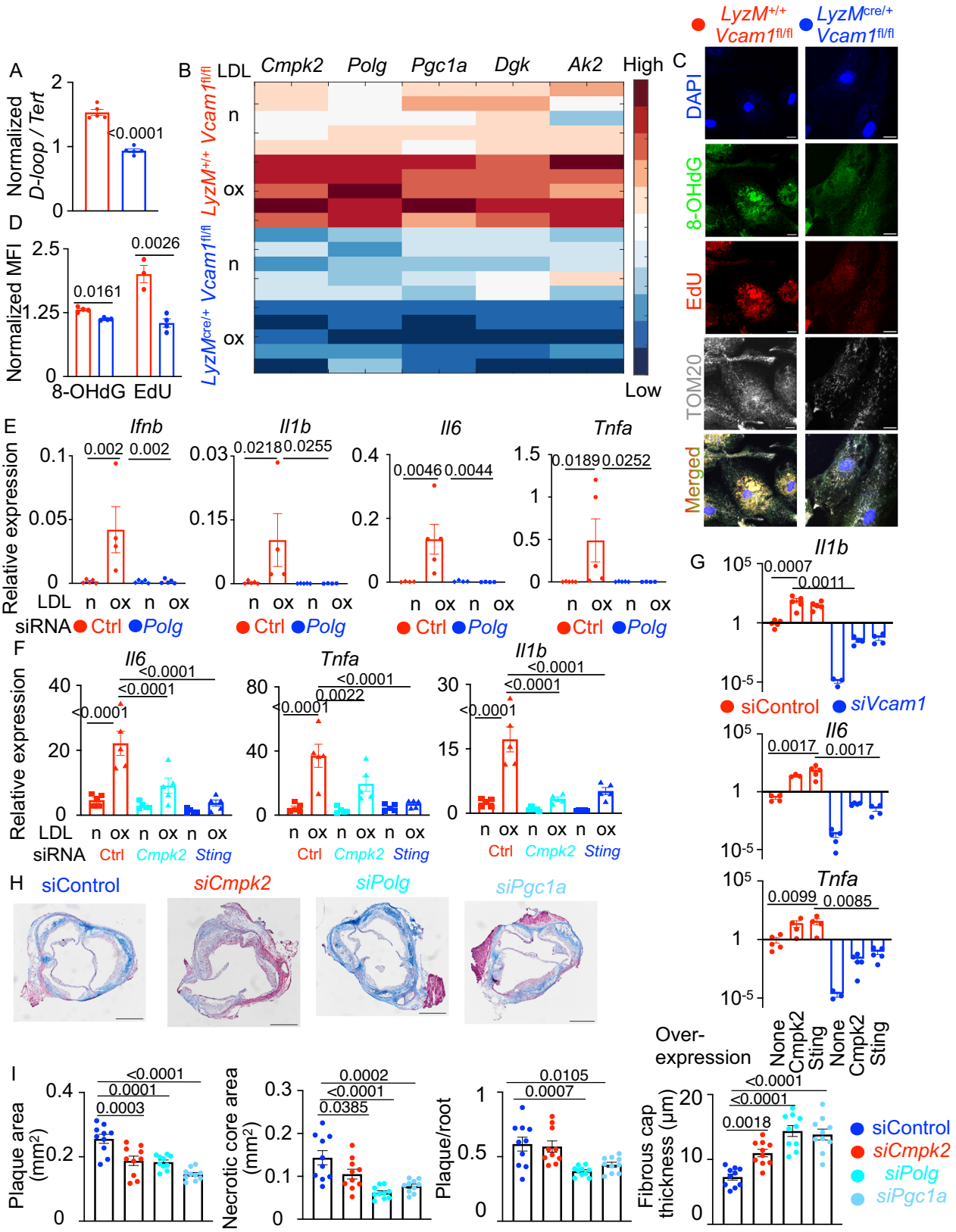

activates cGAS and leads to the production of cyclic GMP–AMP (cGAMP), a second messenger molecule and potent agonist of STING[90–96]. STING can activate and promote NLRP3 localization in endoplasmic reticulum to enhance inflammation[97–99]. Thus, the cGAS-STING pathway has emerged as a critical mechanism for coupling DNA sensing and the induction of powerful innate immune defense programs[100]. Excessive mtDNA synthesis is a prerequisite step in this process.

There are several genes, which orchestrate mtDNA synthesis, such as *PGC1A*, *CMPK2*, and *POLG*. Mutations in *POLG* have been identified in patients with mitochondrial diseases such as Alpers syndrome and ataxia-neuropathy syndromes[101]. Interestingly, a recent study showed

Fig. 4 | VCAM-1 mediates inflammation by enhancing mtDNA synthesis. (**A**-**D**) mtDNA levels by qPCR after oxLDL treatment (**A**, normalized to nLDL, $n = 4$/group, two-tailed t-test), mtDNA synthesis gene expression after nLDL (n) or oxLDL(ox) treatment by qPCR (**B**), and representative 8-OHdG, EdU, and TOM20 images after oxLDL treatment (**C**, scale bar: 20 μm), and 8-OHdG and EdU levels in mitochondria after oxLDL treatment by confocal microscopy (**D**, normalized to nLDL, $n = 4$/group) are shown in $LyzM^{+/+}$ $Vcam1^{fl/fl}$ and $LyzM^{cre/+}$ $Vcam1^{fl/fl}$ BMDM. (**E**) *Polg* was silenced in $LyzM^{+/+}$ $Vcam1^{fl/fl}$ BMDM treated with either nLDL or oxLDL, and the pro-inflammatory genes were measured by qPCR ($n = 5$/group, one-way ANOVA with post-hoc Fisher LSD test). (**F**) *Cmpk2* and *Sting* were silenced in $LyzM^{+/+}$ $Vcam1^{fl/fl}$ BMDM treated with either nLDL or oxLDL, and the pro-inflammatory genes were measured by qPCR ($n = 5$/group, one-way ANOVA with post-hoc Fisher LSD test). (**G**) *CMPK2* and *STING* were overexpressed with a lentiviral vector in THP-1 macrophages treated with either control (siControl $n = 5$) or *VCAM1* siRNA (*siVcam1* $n = 3$-4 no over expression, $n = 4$ *Cmpk2* and *Sting* over expression), and the pro-inflammatory genes were measured by qPCR, one-way ANOVA with post-hoc Fisher LSD test used. (**H**-**I**) *Polg*, *Cmpk2* and *Pgc1a* were silenced selectively in macrophages of female $Ldlr^{-/-}$ mice on atherogenic diet by siRNA delivery in DOTAP liposomes for 8 weeks. Representative images of Masson's trichrome-stained aortic root sections are shown (scale bar: 200 μm). One-way ANOVA with post-hoc Fisher LSD test, $n = 5$/group). All bar graphs shown as mean ± SEM.

that CMPK2 is necessary for the generation of oxidized mtDNA, which, in turn, triggers NLRP3 inflammasome activation[101,102]. Metformin, which is an anti-diabetic drug, was successfully used to reduce mtDNA synthesis and COVID-19-induced acute respiratory distress syndrome[103]. Oxidized and fragmented mtDNA release from the mitochondria into the cytoplasm is crucial to subsequent inflammatory steps[29]. Besides activating STING, breaks in mtDNA trigger a RIG-I-MAVS-dependent immune response, increase the expression of type I interferon stimulated genes, and enhance immune surveillance[104]. In the present study, we showed that the adhesion molecule VCAM-1 increases the expression of C/EBPa that binds to the promoter region of *Cmpk2*, augmenting its expression. We also observed that oxidized and fragmented mtDNA triggers the activation of cGAS-STING pathway-dependent inflammation and aggravates atherosclerosis. However, it is not clear exactly how mtDNA gets oxidized in atherosclerotic conditions. A tempting hypothesis is that mitochondrial ROS produced due to inflammatory and noxious microenvironment in atheromas oxidizes mtDNA. Mitochondria are the major cellular sources of ROS production under physiological conditions[105,106], and mtDNA synthesis and metabolism further augment cellular ROS production[107,108]. Various studies showed that increased mitochondrial ROS generation and dysfunction are associated with inflammatory conditions including cardiovascular diseases[52,53]. Mitochondrial ROS is one of the main causes of mtDNA damage and may induce leakage of mtDNA into the cytosol[61]. In line with these reports, we observed that $Vcam1^{-/-}$ BMDM had reduced mitochondrial ROS compared to $Vcam1^{+/+}$ BMDM, and mitoTEMPO, a mitochondrial ROS scavenger, significantly lowered the expression of inflammatory genes in $Vcam1^{+/+}$ BMDM in response to oxLDL. Furthermore, our study does not elucidate the mechanisms of mtDNA escape into the cytoplasm in atherosclerosis. A very recent study elegantly demonstrated that LPS-induced exit of mtDNA from the mitochondria relies on mPTP and VDAC-dependent channels[109]. Whether macrophages present in atheromas use the same mechanisms remains to be investigated.

In addition to fragmented and oxidized mtDNA, exaggerated mitochondrial oxidative phosphorylation can kindle inflammation. Whether VCAM-1-amplified mitochondrial metabolism stimulates inflammation and atherogenesis, independent of mtDNA sensing by STING, is beyond the scope of this study. The elegant study by Chen et al. demonstrated that oxLDL treatment induces a CD36-dependent metabolic switch from mitochondrial oxidative phosphorylation to glycolysis[110]. Although we found enhanced glycolysis in BMDM after oxLDL treatment, we also observed elevated mitochondrial oxidative phosphorylation in response to this stimulus. A possible explanation of this discrepancy is that the study by Chen et al. used peritoneal macrophages whereas we used BMDM for the seahorse assay. Since macrophage niche determines the epigenetic landscapes and functions of this cell population[111], the difference seen in OCR in our study could be attributed to the fact that we cultured bone marrow cells in vitro over seven days to obtain macrophages. This is also supported by a study showing that oxLDL treatment confers discrete inflammatory and metabolic responses in BMDM and peritoneal macrophages[112]. Additionally, the generation of anti-inflammatory alternative macrophages in response to oxLDL treatment in BMDM due to PPARα and PPARγ activation has been reported[113,114].

We observed that the atheroprotective effects of VCAM-1 deficiency were due to elevated expression of *FCOR* and *LYZ1*, resulting in dampened inflammation. *FCOR* is a repressor that regulates insulin sensitivity and energy metabolism by acting to fine-tune FOXO1 activity[115], and *LYZ1* has antibacterial properties[116]. Our data showed that these genes are controlled by the genes regulating mtDNA synthesis, such as *POLG* and *CMPK2*. However, we do not know how exactly these genes alter the expression of *FCOR* and *LYZ1*. Furthermore, although we observed macrophages lacking these genes are less inflammatory, our study did not ascertain the mechanisms behind this. Additionally, we observed that, in contrary to the anti-inflammatory effects of *Wisp2*, the deficiency of this gene in macrophages thickened the fibrous cap in atherosclerotic lesions, indicating its role in plaque vulnerability. However, how exactly *Wisp2* exerts anti-inflammatory and pro-atherogenic effects is not clear. Future studies will be required to investigate the mechanisms.

Despite aggressive cholesterol-lowering therapy, a group of patients with atherosclerosis have high mortality due to residual inflammation[117]. Cellular metabolism, which is causally linked with inflammation, has been targeted to reduce cardiovascular pathogenesis[18,118–122]. The present work delineates VCAM-1 expression by plaque macrophages as an essential contributor of inflammation and atherosclerosis development and proposes an urgent need in targeting mtDNA synthesis in atherosclerosis.

Methods

Our research complies with all relevant ethical regulations and were approved by the University of Pittsburgh Institutional Animal Care and Use Committee.

Animals

All animal experiments were performed according to the NIH guidelines, and the protocols of the animal experiments were approved by the University of Pittsburgh Institutional Animal Care and Use Committee. The mice were housed in 12 hour dark/light cycle at 70° F and 40% humidity. Adult C57BL/6 wild-type (#000664), $LyzM^{cre/cre}$ (#004781), $Sting^{fl/fl}$ (#031670), $Apoe^{-/-}$ (#002052) and $Ldlr^{-/-}$ (#002207) mice were obtained from the Jackson laboratory. $Cmpk2^{fl/fl}$ mice were obtained from MRC Harwell Institute, UK. $Vcam1^{fl/fl}$ mice were generous gifts from Dr. Thalia Papayannopoulou, University of Washington. Myeloid-specific deletion of *Vcam1* was generated by breeding $Vcam1^{fl/fl}$ mice with $LyzM^{cre/cre}$ mice. $ApoE^{-/-}$ $Vcam1^{fl/fl}$ $LyzM^{Cre/+}$ mice were generated by breeding $Vcam1^{fl/fl}$ $LyzM^{Cre/+}$ and $ApoE^{-/-}$ mice. All animals were maintained in a standard 12-hour light/ dark cycle in the vivarium. Ten to twelve-week-old mice were fed with an atherogenic diet composed of 21% milk fat and 0.2% cholesterol (0.15% added, 0.05% from milk fat) (Teklad) for 16 weeks and then sacrificed. Bone marrow was collected for flow cytometry or BMDM culture. Spleen and blood were collected for flow cytometry. Aortas were excised for flow cytometry and immuno-imaging. Age-matched litter mate controls were used in each experiment.

https://doi.org/10.1038/s41467-024-51780-1

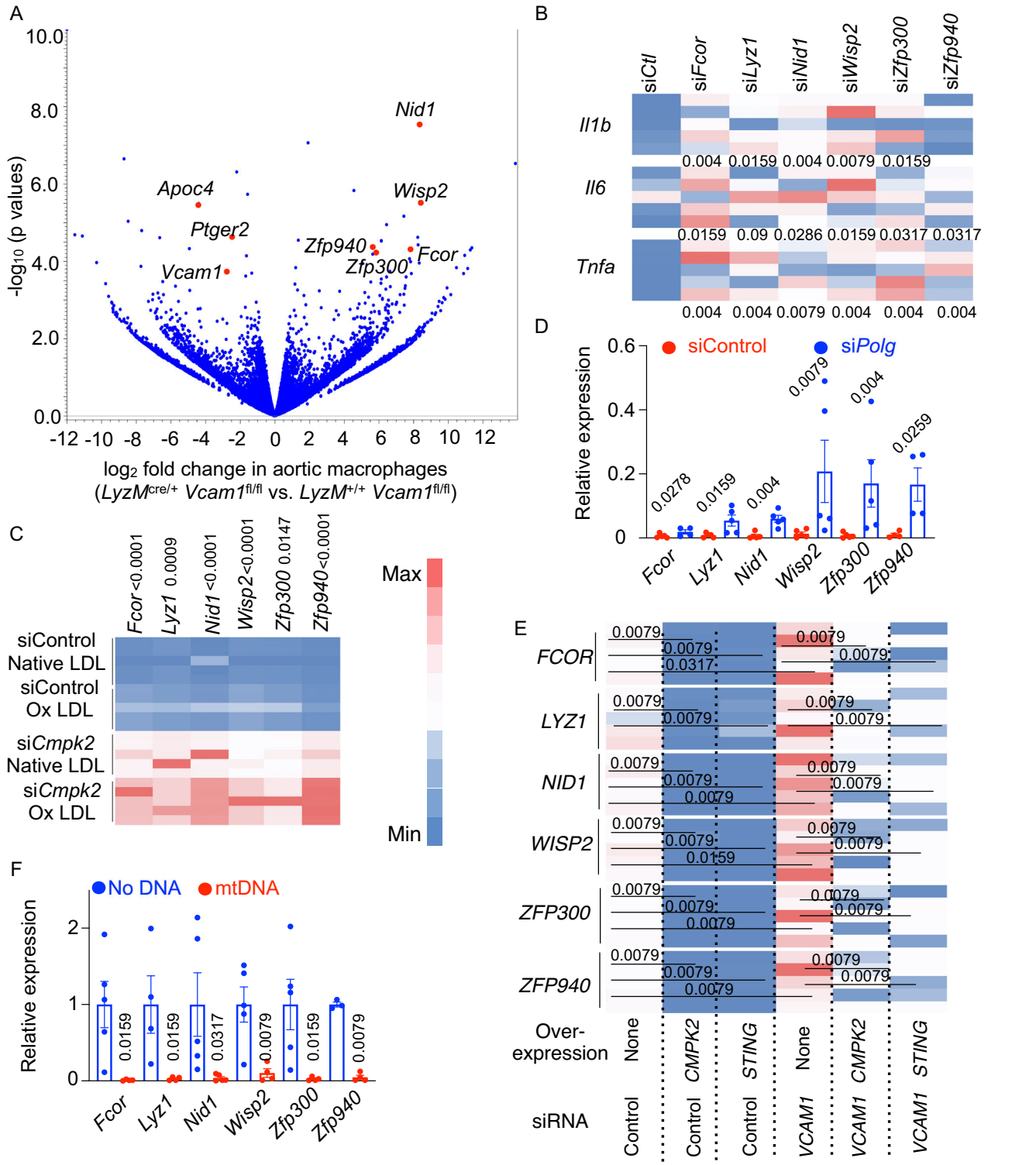

Fig. 5 | VCAM-1-mediated mtDNA synthesis regulates the downstream genes. **A** Female *Ldlr*$^{-/-}$ mice were lethally irradiated, transplanted with either *LyzM*$^{+/+}$ *Vcam1*$^{fl/fl}$ or *LyzM*$^{cre/+}$ *Vcam1*$^{fl/fl}$ bone marrow cells, and fed with a high fat diet for four months. RNA sequencing was performed with aortic macrophages isolated from these mice. The volcano plot shows the key differentially expressed genes ($n = 3$/group) in aortic macrophages, data plotted as $\log_2$(fold change) vs. $\log_{10}$(FDR corrected P-value). **B** The expression of the inflammatory genes after silencing the VCAM-1 downstream genes in BMDM treated with oxLDL was measured by qPCR in *LyzM*$^{+/+}$ *Vcam1*$^{fl/fl}$ BMDM cultured in presence of either native or oxidized LDL ($n = 5$/group, one-tailed Mann-Whitney test). **C, D** The VCAM-1 downstream genes were measured after silencing *Cmpk2* (**C**) and *Polg* (**D**). **C, D:** $n = 5$/group, one-way ANOVA with post-hoc Fisher LSD test. **E** *CMPK2* and *STING* were overexpressed with a lentiviral vector in THP-1 macrophages treated with either control or *VCAM1* siRNA. The VCAM-1 downstream genes were measured by qPCR ($n = 5$/group, two-tailed Mann-Whitney test). **F** The VCAM-1 downstream genes were quantified after mtDNA transfection in *LyzM*$^{+/+}$ *Vcam1*$^{fl/fl}$ BMDM treated with oxidized LDL ($n = 5$/group, Two-tailed Mann-Whitney test). All bar graphs shown as mean ± SEM.

https://doi.org/10.1038/s41467-024-51780-1

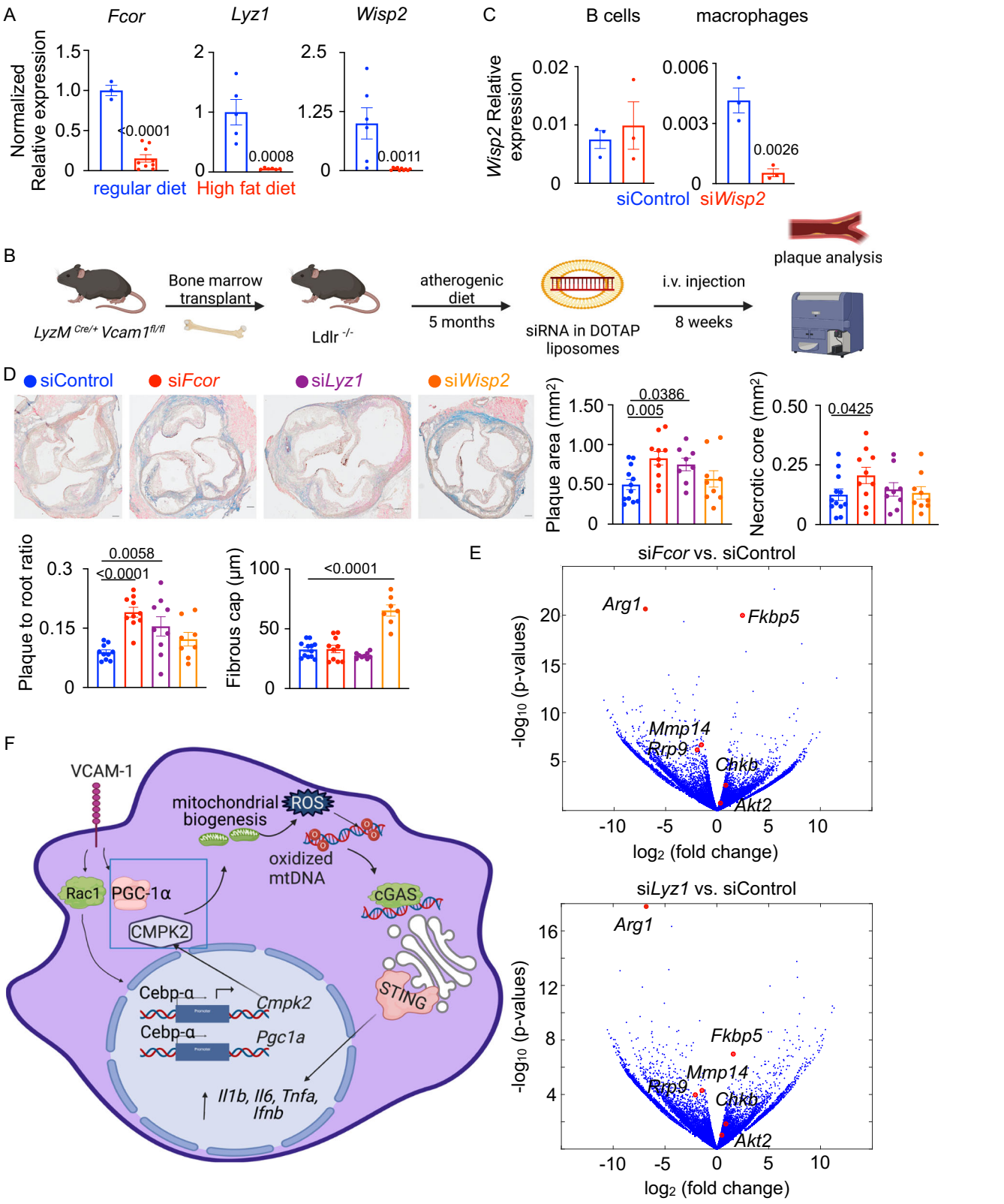

In vivo gene silencing with DOTAP

Ldlr$^{-/-}$ mice were irradiated and transplanted with bone marrow from LyzM$^{Cre/+}$ *Vcam1*$^{fl/fl}$ mice followed by administration of atherogenic diet for five months. The mice were randomized into 4 cohorts and si*Control*, si*Lyz1*, si*Fcor*, and si*Wisp2* were administered intravenously in DOTAP liposomes weekly for the last 8 weeks of the experiment. 50:50 DOTAP:cholesterol liposomes (Encapsula Nanosciences), were administered at 1:7.5 siRNA:total DOTAP by weight and a dosage of 1.5 mg/kg DOTAP.

Fig. 6 | VCAM-1 inhibits Fcor and Lyz1 to promote atherosclerosis. A Expression of *Fcor*, *Lyz1*, and *Wisp2* in sorted aortic macrophages from *Apoe*$^{-/-}$ mice on regular and atherogenic diet was quantified by qPCR ($n = 4$/group, two-tailed Student's t-test. **B** The experimental schematic has been shown. Female *Ldlr*$^{-/-}$ mice were lethally irradiated, transplanted with *LyzM*$^{cre/+}$ *Vcam1*$^{fl/fl}$ bone marrow cells, and fed a high fat diet for five months. The animals were randomized into 4 groups, and siRNA (siControl, si*Fcor*, si*Lyz1*, and si*Wisp2*) in DOTAP nanoparticles was administered intravenously for 8 weeks. **C** In vivo gene silencing by siRNA-DOTAP delivery has been validated. $n = 3$/group, two-tailed Student's t-test. **D** The representative images and quantification of different parameters of aortic root sections of siControl, si*Fcor*, si*Lyz1*, and si*Wisp2*-treated mice have been shown, scale bar: 100 μm. $n = 5$/group, one-way ANOVA with post-hoc Fisher LSD test. **E** The volcano plots depict differentially expressed genes in aortic macrophages of si*Fcor* and si*Lyz1* vs. siControl-treated mice ($n = 5$/group), data plotted as $\log_2$(fold change) vs. $\log_{10}$(FDR corrected *P*-value). **F** Schematic representation of VCAM-1 signaling in macrophages is shown (Biorender). All bar graphs shown as mean ± SEM.

Organ harvesting and flow cytometry

Mice were euthanized according to the University of Pittsburgh IACUC guidelines followed by perfusion of PBS through the left ventricle. Aortas were harvested, minced, and digested in 450U/ml collagenase I (sigma C0130), 125U/ml collagenase XI (Sigma), 60U/ml DNase I (Worthington), 60U/ml hyaluronidase (Sigma-Aldrich), and 20 μM HEPES at 37 °C at 750 rpm for 20 minutes. The dissociated cell suspension was passed through 70 μM cell strainers and resuspended in FACS buffer (PBS + 0.5%BSA) after centrifugation. Blood was collected by terminal cardiac puncture and incubated with RBC lysis buffer for 3 minutes at room temperature, followed by the addition of FACS buffer and centrifugation to pellet leukocytes. A hemocytometer was used to count the number of viable cells in the organs.

The following panel of antibodies were used to analyze the myeloid cell population in mice: anti-CD45.2 (Biolegend 109820, clone 104, lot B364148), CD11b (BD Biosciences 557657, clone M1/70, lot 1271559), CD115 (Biolegend 565249, clone T38-320, lot 7291701), Ly6G (Biolegend 563979, clone 1A8, lot 0269936), Ly-6C (eBioscience 45-5932-82, clone HK1.4, lot 2162018), F4/80 (Biolegend 123114, clone BM8, lot B370041) CD3 (BD Biosciences 367-0032-82, clone 17A2, lot 2526889), and CD19 (BD Biosciences 563148, clone 1D3, lot 3130912). In addition, VCAM-1 (Biolegend 105704, clone 429, lot B173769), Streptavidin-BV510 (BD Biosciences 563261, lot 8010877), Siglec (eBioscience 17-5833-82, clone SH2.1, lot E17250-102) and IL-4 (Biolegend 504124, clone 11B11, lot B374781) antibodies were used for flow cytometry. Neutrophils were identified as CD11b$^+$, Ly6G$^+$, and CD115$^-$. Monocytes were considered as CD11b$^+$, Ly-6G$^-$, and CD115$^+$. Lymphocytes B and T were identified as CD11b$^-$, CD19$^+$, CD3$^-$ and CD11b$^-$, CD19$^-$, CD3$^+$ respectively. Aortic macrophages were determined as CD45.2$^+$, CD11b$^+$, Ly6G$^-$, and F4/80$^+$, and sorted into Picopure (Thermo Scientific) extraction buffer for RNA sequencing and qPCR. Eosinophils were identified as CD45$^+$ CD11b$^-$ Siglec$^+$. Th2 cells were identified as CD45$^+$ CD3$^+$ CD4$^+$ IL4/5$^+$. A Fortessa flow cytometer (BD) or cytek Aurora flow cytometer were used to acquire the data, which were analyzed with FlowJo software (Tree Star).

Histology, immunofluorescence, and western blotting

Aortic roots were excised after PBS perfusion and embedded in OCT compound (Sakura Finetek) on dry ice. Sections (10uM) were cut using a cryostat at three levels for quantification of plaque burden[123], and Masson Trichrome staining was performed to quantify plaque size as follows. Aortic root sections were fixed overnight in Bouin's fixative (RT). Slides were washed in tap water to remove residual Bouin's fixative, then stained for 10 minutes with a 1:1 mixture of hematoxylin A and B (Thermo Scientific). Next, the slides were incubated in scarlet acid stain (Electron Microscopy Sciences) for 10 minutes, followed by 5 minutes in phosphomolybdic acid solution (Electron Microscopy Sciences). Finally, the sections were stained with aniline blue solution (Electron Microscopy Sciences) for 5 minutes and then transferred to 1% acetic acid for 5 minutes, dehydrated in ethanol and xylene, and mounted in permount (Electron Microscopy Sciences), cured for 24 hours before imaging. Stained sections were imaged using Nikon A1, a confocal microscope, at the University of Pittsburgh Center for Biological Imaging. Total plaque area, necrotic core area, and fibrous cap thickness were calculated using ImageJ (NIH). NSPARC imaging was performed on a Nikon AX-R confocal with a Nikon Spatial Array Confocal (NSPARC) detector equipped with a 40X objective.

Deidentified human carotid arteries were obtained in collaboration with Dr. Leers (IRB approvals: STUDY19020234 and PRO18060512, control arteries and advanced plaques from patients who underwent endarterectomy) and NDRI (early plaques from diseased patients). Informed consent is not applicable for the deidentified carotid artery samples obtained, hence patient clinical information is not available. Carotid artery samples were fixed, and embedded in OCT compound for immunostaining and FFPE blocks for histological staining. OCT blocks were sectioned (10 μm), and sections were permeabilized with 0.1% Triton X-100 in PBS prior to staining with 8-OHdG (Novus), VCAM-1 (Invitrogen), TOM20 (Abcam), and CD68 (Abcam) antibodies. Sections were imaged with a Nikon A1 confocal microscope. Images were quantified in a randomized, blinded manner using ImageJ (NIH) to enumerate VCAM-1, TOM20, CD68, and 8-OHdG MFI, and necrotic core areas. Correlation analyzes were performed using GraphPad.

Mouse aortic roots were embedded in OCT compound, sectioned, and permeabilized with 0.1% Triton X-100 in PBS prior to staining with malondialdehyde (Abcam ab27642), CCR2 (eBioscience), iNos (Invitrogen/eBioscience 14-5920-82) antibdodies. BMDM were cultured in chamber slides for immunofluorescence images and stained with dsDNA (Abcam ab27156), Tfam (ThermoFisher/Proteintech 22586-1-AP).

Mitochondrial complexes and Parkin western blot: 200,000 BMDMs were plated per well in a 6-well plate and treated with nLDL or oxLDL for 96 hours. BMDM were then lysed in 1X RIPA buffer with protease inhibitor cocktail (Roche). 6X Laemmli buffer was added and the lysates were run on a 10% SDS-PAGE, transferred to a nitrocellulose membrane, blocked with 5% BSA, and probed with antibodies (Parkin: Novus Bio, mitochondrial complexes: Abcam, pSting: Cell Signaling, Sting: Cell Signaling) prior to chemiluminescent imaging with ECL. B-actin was used as loading control. Moreover, TOM20 was used to control for mitochondrial mass. Bands were quantified using ImageJ. The uncropped images of the western blots have been included in a supplemental file.

Liquid chromatography-high resolution mass spectrometry and ^{13}C glucose flux

Sample preparation: Metabolic quenching and polar metabolite pool extraction was performed using ice cold 80% methanol in water with 0.1% formic acid at a ratio of 500 μL per 1e6 cells. A mix of stable isotope labeled internal standards including taurine-$_{d4}$, lactate-$_{d3}$, alanine-$_{d3}$, and ^{13}C-creatinine (Sigma-Aldrich) was added to the cell lysates for a final concentration of 10 μM. The supernatant was cleared of protein by centrifugation at 16,000 x *g*. A total of 400 μL of cleared supernatant was dried under nitrogen gas and resuspended in 40 μL water for online LC-MS analysis.

LC-HRMS method: Samples (2 μL) were injected via a Thermo Vanquish UHPLC and separated over a reversed phase Thermo HyperCarb porous graphite column (2.1 × 100 mm, 3μm particle size) maintained at 55 °C. For the 20 min LC gradient, the mobile phase consisted of the following: solvent A (water/0.1% FA) and solvent B (ACN/0.1% FA). The gradient was the following: 0-1 min 1% B with an increase to 15%B over 5 min, continue increasing to 98% B over 5 min

and holding at 98% B for 5 min, followed by equilibration at 1% B for 5 min. The Thermo ID-X tribrid mass spectrometer was operated in negative ion mode, scanning in ddMS^2 mode (2 µscans) from 70 to 800 *m/z* at 120,000 resolution with an AGC target of 2e5 for full scan, 2e4 for MS^2 scans using HCD fragmentation at stepped 15,35,50 collision energies. Source ionization was set to 2.4 kV spray voltage. Source gas parameters were 35 sheath gas, 12 auxiliary gas at 320 °C, and 8 sweep gas. Calibration was performed prior to analysis using the Pierce™ FlexMix Ion Calibration Solutions (Thermo Fisher Scientific). Peak areas were manually extracted using Thermo QuanBrowser ver4.3, normalized to internal standards. Background natural ^{13}C abundance of isotopologues were subtracted out using the MIMOSA technique[124], before graphing using GraphPad PRISM 9.0.

Luminex
Biomarkers were analyzed using a Bio-Rad mouse 23-plex and a Bio-plex 200 (Bio-Rad). Serum samples were diluted 5-fold using diluent provided by the company and analyzed in duplicates. Cell culture supernatants were analyzed as neat and run in single. Standard curve and experimental data were generated and analyzed using the Bio-Plex Manager Software.

Bioenergetic Measurements
Isolated macrophages were seeded in the Seahorse XF24 microplate and treated with 100µg/ml nLDL or oxLDL for 96 hours. Oxygen Consumption Rate (OCR) and Extracellular Acidification Rate (ECAR) were measured by XF analysis (XF24, Agilent Seahorse Technologies). After measurement of basal OCR, 2.5 µmol/L oligomycin A, 1.0 µmol/L FCCP (to measure maximal OCR), and 10 µmol/L rotenone and Antimycin A were consecutively added. Reserve capacity was calculated by subtracting basal OCR from maximal OCR. ATP-linked OCR was calculated by subtracting proton leak from basal OCR. All rates were normalized to the number of macrophages measured by crystal violet staining.

Electron transport chain complex activity
Enzymatic activity of complexes I, II, III, IV, and V and citrate synthase were performed by spectrophotometric kinetic assays according to manufacturer's guidelines[125,126].

RT-PCR
RNeasy RNA isolation kit (Qiagen) was used to extract RNA from bone marrow-derived macrophages, and cDNA was synthesized using Applied Biosystems High Capacity RNA to cDNA kit. Gene expression was quantified by quantitative RT-PCR using SYBR green mastermix, and primers (IDT). Gene expression Ct values were normalized to those of β-actin. Heat maps were generated with MATLAB and Excel. The list of the primers used in this study is included in Table S11. *In-vitro BMDM chemotaxis assay*

Chemotaxis assay was performed using Ibidi µ-Slide chemotaxis protocol. Briefly, BMDM from *LyzM*$^{Cre/+}$ *Vcam1*$^{fl/fl}$ and *LyzM*$^{+/+}$ *Vcam1*$^{fl/fl}$ animals were seeded at a concentration of 3×10^6 cells/mL and embedded into a gel. They were then injected into the µ-Slide (Ibidi, cat #80326). The cells were then incubated at 37° C until the gel was formed. Finally, a chemottractant was added to the µ-Slide and video microscopy was conducted at the Center for Biologic Imaging at the University of Pittsburgh.

BMDM culture, oxidized LDL, and siRNA treatment
Bone marrow cells were isolated from the femurs and tibias of *LyzM*$^{+/+}$ *Vcam1*$^{fl/fl}$ and *LyzM*$^{Cre/+}$ *Vcam1*$^{fl/fl}$ mice after euthanasia followed by intracardiac perfusion using PBS. The cells were cultured in DMEM (low glucose) containing 5.5 mM glucose and supplemented with 20% L929 conditioned medium. The cells were seeded in 12 well plates. After the cells were 80% confluent, the culture was treated with 100 µg/ml concentrations of native or oxidized LDL (BioLegend) for 48 hours. For gene silencing, cells were seeded in 6-well plates. We replaced the cell culture media with DMEM containing no FBS and antibiotics when the cells were 80% confluent. Then the cells were treated with 50 µl of OPTI-MEM (Gibco) containing 3 µl of Lipofectamine 2000 (Invitrogen) and 50 nM of either control, or si*RNA* against the gene of interest (IDT). After 12 hours, cell culture medium was removed, and the cells were incubated with DMEM medium containing L929- conditioned medium for 72 hours before analysis.

mtDNA and nuclear DNA transfection
Mitochondrial DNA was isolated from the liver using mitochondrial DNA extraction kit (Abcam ab65321). Isolated mitochondrial DNA was transfected in BMDM using lipofectamine as per manufacturer's protocol[102].

mitoTEMPO treatment
BMDM were treated with 100 µM mitoTEMPO for 1 hour prior to oxLDL treatment (48 hours).

mDNA depletion
Mitochondrial DNA was depleted in BMDM using 1 µM ddC[127]. ddC was added to the culture medium for 5 days to deplete mitochondrial DNA. The cells were stimulated with 100 µg/ml oxLDL following mitochondrial DNA depletion and inflammatory gene expression was elucidated by qPCR.

RNA isolation and sequencing
RNA was isolated according to the manufacturer's protocol. Library prep and sequencing were performed by the Health Science Sequencing core at UPMC Children's Hospital, Pittsburgh. RNA quality was assessed on an Agilent TapeStation 2200 using the High Sensitivity RNA Tape (Agilent: 5567-5579). 5.5 µl of each sample was used for cDNA generation using the Takara Smart-Seq HT kit (Takara: 634438) following manufacturer instructions, with 15 cycles of cDNA amplification. Smart-Seq cDNA was assessed for quality on an Agilent TapeStation 2200 using the D5000 High sensitivity ScreenTape (Agilent: 5067-5592). All samples passed QC with full-length cDNA and proceeded to library preparation using Illumina Nextera XT kit (Illumina: FC-131-1096) using 12 PCR cycles. Libraries were pooled and sequenced on an Illumina NextSeq 500 using a High Output 150 v2.5 cycle flow cell (Illumina: 20024907), 2 × 75 bp, for an average of ~40 million reads per sample.

RNA-sequencing data analysis
CLC genomics workbench was used to analyze transcriptomic data generated by RNA sequencing. The data generated from our RNAseq experiments have been deposited to GEO (GSE207634 and GSE266296) and will be publicly released after the official acceptance of this manuscript. The FASTQ files provided by Health Science Sequencing Core at UPMC Children's Hospital were imported into CLC Genomics Workbench 22. A sequencing QC report was generated to assess data quality. A PHRED score of less than 40 is considered optimal for downstream analysis. The adapter present at the 3′ end of the sequences was trimmed. The trimmed reads were aligned to the *Mus musculus* CLC reference genome version 86. The gene expression was calculated as reads per kilobase of transcript per million mapped reads (RPKM). Next, differential expression of genes in *Vcam1*$^{-/-}$ and *Vcam1*$^{+/+}$ aortic macrophages was calculated. Differentially expressed genes were identified with at least 2 log2 fold change and FDR-corrected p value < 0.05.

Spatial transcriptomics (Curio Slideseq)
Aortic root sections (10 µm) of *LyzM*$^{+/+}$ *Vcam1*$^{fl/fl}$ and *LyzM*$^{Cre/+}$ *Vcam1*$^{fl/fl}$ animals on HFD for 5 months were cut and melted onto Slide-seq

arrays. Next, the arrays with captured sections were transferred to a 1.5 ml tube of hybridization buffer (6× sodium chloride sodium citrate with 2 U μl^{-1} Lucigen NxGen RNAse inhibitor) for 30 min. Libraries were generated and sequenced according to the Slideseq-V2 protocol. The data have been deposited to the GEO (GSE266296).

Pre-processing of Slide-seq reads: Reads were aligned to GRCm39.103 and processed using Slide-seq pipeline to generate gene count matrix and match array barcode and sequenced reads. Seurat was employed for the quality control, normalization, and clustering analyzes.

Cell type deconcolution of Slide-seq data using Robust Cell Type Deconvolution (RCTD)

Cell type deconvolution of Slide-seq data was performed using RCTD[128]. Single-cell RNA-seq reference data from abdominal aortic cells were utilized[44]. Quality control, normalization, and clustering analyzes were conducted using the Seurat package. Cell types were determined based on key markers identified in Zhao et al. To enhance deconvolution quality, the reference dataset was limited to the predominant cell types: macrophages (4 sub-clusters), fibroblasts (2 sub-clusters), and smooth muscle cells (2 sub-clusters). RCTD was executed in doublet mode, given the Curio Slide-seq's high resolution, with a Unique Molecular Identifier (UMI) threshold of 50 for default-aligned samples and 10 for short-read-aligned samples. Subsequent analyzes included regions exclusively identified as macrophages with a weight ≥ 0.6 or as two cell types with a macrophage weight ≥ 0.6.

Differentially expressed gene analyzes

For downstream differentially expressed gene (DEG) analysis, six Slide-seq datasets, formatted as Seurat objects, were integrated using the SCTransform pipeline of Seurat. The confidently labeled macrophage regions were extracted from the integrated Seurat object, control samples within the macrophage population, and its sub-clusters.

Over-representation analyzes of DEGs

Over-representation analysis (ORA) of DEGs was conducted using the WebGestalt online toolkit[129]. DEGs with an adjusted p-value > 0.05 or an absolute log2 fold change <1 were excluded. The murine canonical pathways database from MsigDB served as the functional database for the analysis.

Statistical analysis

Data are displayed as mean ± SEM. Statistical significance between groups was performed using Graphpad PRISM with Mann-Whitney, Student's t-test or ANOVA according to the dataset. Results were considered as statistically significant when $p < 0.05$.

Reporting summary

Further information on research design is available in the Nature Portfolio Reporting Summary linked to this article.

Data availability

The RNAseq (bulk and spatial) data generated in this study have been deposited in GEO – bulk RNAseq GSE266296, spatialRNAseq GSE20764 (https://www.ncbi.nlm.nih.gov/geo/query/acc.cgi?acc=GSE207634). The raw data are available from the corresponding author upon request. Source data are provided with this paper.

References

1. Xu, T. et al. Metabolic control of T(H)17 and induced T(reg) cell balance by an epigenetic mechanism. *Nature* **548**, 228–233 (2017).
2. O'Neill, L. A. & Pearce, E. J. Immunometabolism governs dendritic cell and macrophage function. *J. Exp. Med* **213**, 15–23 (2016).
3. Desdin-Mico, G. et al. T cells with dysfunctional mitochondria induce multimorbidity and premature senescence. *Science* **368**, 1371–1376 (2020).
4. Iwata, R., Casimir, P. & Vanderhaeghen, P. Mitochondrial dynamics in postmitotic cells regulate neurogenesis. *Science* **369**, 858–862 (2020).
5. Wang, Y. et al. Mitochondrial fission promotes the continued clearance of apoptotic cells by macrophages. *Cell* **171**, 331–345.e322 (2017).
6. Minhas, P. S. et al. Restoring metabolism of myeloid cells reverses cognitive decline in ageing. *Nature* **590**, 122–128 (2021).
7. Liu, J. et al. CCR7 Chemokine Receptor-Inducible lnc-Dpf3 Restrains Dendritic Cell Migration by Inhibiting HIF-1α-Mediated Glycolysis. *Immunity* **50**, 600–615.e615 (2019).
8. DeBerge, M. et al. Hypoxia-inducible factors individually facilitate inflammatory myeloid metabolism and inefficient cardiac repair. *J. Exp. Med.* **218**, e20200667 (2021).
9. Lee, J. et al. Regulator of fatty acid metabolism, acetyl coenzyme a carboxylase 1, controls T cell immunity. *J. Immunol.* **192**, 3190–3199 (2014).
10. Berod, L. et al. De novo fatty acid synthesis controls the fate between regulatory T and T helper 17 cells. *Nat. Med.* **20**, 1327–1333 (2014).
11. Schulthess, J. et al. The short chain fatty acid butyrate imprints an antimicrobial program in macrophages. *Immunity* **50**, 432–445.e437 (2019).
12. O'Neill, L. A., Kishton, R. J. & Rathmell, J. A guide to immunometabolism for immunologists. *Nat. Rev. Immunol.* **16**, 553–565 (2016).
13. Weinberg, S. E. et al. Mitochondrial complex III is essential for suppressive function of regulatory T cells. *Nature* **565**, 495–499 (2019).
14. Faas, M. et al. IL-33-induced metabolic reprogramming controls the differentiation of alternatively activated macrophages and the resolution of inflammation. *Immunity* **54**, 2531–2546.e2535 (2021).
15. Carroll, R. G. et al. An unexpected link between fatty acid synthase and cholesterol synthesis in proinflammatory macrophage activation. *J. Biol. Chem.* **293**, 5509–5521 (2018).
16. Lauterbach, M. A. et al. Toll-like receptor signaling rewires macrophage metabolism and promotes histone acetylation via ATP-Citrate Lyase. *Immunity* **51**, 997–1011 e1017 (2019).
17. Covarrubias, A. J. et al. Akt-mTORC1 signaling regulates Acly to integrate metabolic input to control of macrophage activation. *Elife* **5**, e11612 (2016).
18. Baardman, J. et al. Macrophage ATP citrate lyase deficiency stabilizes atherosclerotic plaques. *Nat. Commun.* **11**, 6296 (2020).
19. Huang, S. C. et al. Cell-intrinsic lysosomal lipolysis is essential for alternative activation of macrophages. *Nat. Immunol.* **15**, 846–855 (2014).
20. Keiran, N. et al. SUCNR1 controls an anti-inflammatory program in macrophages to regulate the metabolic response to obesity. *Nat. Immunol.* **20**, 581–592 (2019).
21. Cai, S. et al. Mitochondrial dysfunction in macrophages promotes inflammation and suppresses repair after myocardial infarction. *J. Clin. Invest* **133**, e159498 (2023).
22. Cao, Y. et al. Sex differences in heart mitochondria regulate diastolic dysfunction. *Nat. Commun.* **13**, 3850 (2022).
23. Valero, T. Mitochondrial biogenesis: pharmacological approaches. *Curr. Pharm. Des.* **20**, 5507–5509 (2014).
24. Sanchis-Gomar, F., Garcia-Gimenez, J. L., Gomez-Cabrera, M. C. & Pallardo, F. V. Mitochondrial biogenesis in health and disease. Molecular and therapeutic approaches. *Curr. Pharm. Des.* **20**, 5619–5633 (2014).
25. Popov, L. D. Mitochondrial biogenesis: an update. *J. Cell Mol. Med* **24**, 4892–4899 (2020).

26. Handschin, C. & Spiegelman, B. M. Peroxisome proliferator-activated receptor γ coactivator 1 coactivators, energy homeostasis, and metabolism. *Endocr. Rev.* **27**, 728–735 (2006).
27. Evans, M. J. & Scarpulla, R. C. NRF-1: a trans-activator of nuclear-encoded respiratory genes in animal cells. *Genes Dev.* **4**, 1023–1034 (1990).
28. Picca, A. & Lezza, A. M. Regulation of mitochondrial biogenesis through TFAM-mitochondrial DNA interactions: Useful insights from aging and calorie restriction studies. *Mitochondrion* **25**, 67–75 (2015).
29. Riley, J. S. & Tait, S. W. Mitochondrial DNA in inflammation and immunity. *EMBO Rep.* **21**, e49799 (2020).
30. Graziewicz, M. A., Longley, M. J. & Copeland, W. C. DNA polymerase gamma in mitochondrial DNA replication and repair. *Chem. Rev.* **106**, 383–405 (2006).
31. Van Laar, V. S. et al. Evidence for compartmentalized axonal mitochondrial biogenesis: mitochondrial dna replication increases in distal axons as an early response to parkinson's disease-relevant stress. *J. Neurosci.* **38**, 7505–7515 (2018).
32. Golpich, M. et al. Mitochondrial dysfunction and biogenesis in neurodegenerative diseases: pathogenesis and treatment. *CNS Neurosci. Ther.* **23**, 5–22 (2017).
33. Cook-Mills, J. M., Marchese, M. E. & Abdala-Valencia, H. Vascular cell adhesion molecule-1 expression and signaling during disease: regulation by reactive oxygen species and antioxidants. *Antioxid. Redox Signal* **15**, 1607–1638 (2011).
34. Woollard, K. J. & Geissmann, F. Monocytes in atherosclerosis: subsets and functions. *Nat. Rev. Cardiol.* **7**, 77–86 (2010).
35. Kong D. H., Kim Y. K., Kim M. R., Jang J. H. & Lee S. Emerging Roles of vascular cell adhesion molecule-1 (vcam-1) in immunological disorders and cancer. *Int. J. Mol. Sci.* **19**, 1057 (2018).
36. Ley, K. & Huo, Y. VCAM-1 is critical in atherosclerosis. *J. Clin. Invest* **107**, 1209–1210 (2001).
37. Galkina, E. & Ley, K. Vascular adhesion molecules in atherosclerosis. *Arterioscler Thromb. Vasc. Biol.* **27**, 2292–2301 (2007).
38. O'Brien, K. D., McDonald, T. O., Chait, A., Allen, M. D. & Alpers, C. E. Neovascular expression of E-selectin, intercellular adhesion molecule-1, and vascular cell adhesion molecule-1 in human atherosclerosis and their relation to intimal leukocyte content. *Circulation* **93**, 672–682 (1996).
39. Rice, G. E. & Bevilacqua, M. P. An inducible endothelial cell surface glycoprotein mediates melanoma adhesion. *Science* **246**, 1303–1306 (1989).
40. Alon, R. et al. The integrin VLA-4 supports tethering and rolling in flow on VCAM-1. *J. Cell Biol.* **128**, 1243–1253 (1995).
41. Cerutti, C. & Ridley, A. J. Endothelial cell-cell adhesion and signaling. *Exp. Cell Res.* **358**, 31–38 (2017).
42. Sharma, R. et al. Breast cancer metastasis: putative therapeutic role of vascular cell adhesion molecule-1. *Cell Oncol. (Dordr.)* **40**, 199–208 (2017).
43. van Oosten, M., van de Bilt, E., de Vries, H. E., van Berkel, T. J. & Kuiper, J. Vascular adhesion molecule-1 and intercellular adhesion molecule-1 expression on rat liver cells after lipopolysaccharide administration in vivo. *Hepatology* **22**, 1538–1546 (1995).
44. Zhao, G. et al. Single-cell RNA sequencing reveals the cellular heterogeneity of aneurysmal infrarenal abdominal aorta. *Cardiovasc Res* **117**, 1402–1416 (2021).
45. Caligiuri, G. et al. Interleukin-10 deficiency increases atherosclerosis, thrombosis, and low-density lipoproteins in apolipoprotein E knockout mice. *Mol. Med.* **9**, 10–17 (2003).
46. Mallat, Z. et al. Protective role of interleukin-10 in atherosclerosis. *Circ. Res* **85**, e17–e24 (1999).
47. Hamada, M. et al. MafB promotes atherosclerosis by inhibiting foam-cell apoptosis. *Nat. Commun.* **5**, 3147 (2014).
48. Hasegawa, H. et al. The role of macrophage transcription factor MafB in atherosclerotic plaque stability. *Atherosclerosis* **250**, 133–143 (2016).
49. Jagavelu, K. et al. Systemic deficiency of the MAP kinase-activated protein kinase 2 reduces atherosclerosis in hypercholesterolemic mice. *Circ. Res.* **101**, 1104–1112 (2007).
50. Ozcan, L. et al. Allosteric MAPKAPK2 inhibitors improve plaque stability in advanced atherosclerosis. *PLoS One* **16**, e0246600 (2021).
51. Gropen, T. I., Prohovnik, I., Tatemichi, T. K. & Hirano, M. Cerebral hyperemia in MELAS. *Stroke* **25**, 1873–1876 (1994).
52. Anan, R. et al. Cardiac involvement in mitochondrial diseases. a study on 17 patients with documented mitochondrial DNA defects. *Circulation* **91**, 955–961 (1995).
53. Wallace, D. C. Mitochondrial diseases in man and mouse. *Science* **283**, 1482–1488 (1999).
54. Peng, W. et al. Mitochondrial dysfunction in atherosclerosis. *DNA Cell Biol.* **38**, 597–606 (2019).
55. Venditti, P., Di Stefano, L. & Di Meo, S. Mitochondrial metabolism of reactive oxygen species. *Mitochondrion* **13**, 71–82 (2013).
56. Mailloux, R. J. An update on mitochondrial reactive oxygen species production. *Antioxidants* **9**, 472 (2020).
57. Bories, G. F. P. & Leitinger, N. Macrophage metabolism in atherosclerosis. *FEBS Lett.* **591**, 3042–3060 (2017).
58. Pickles, S., Vigié, P. & Youle, R. J. Mitophagy and quality control mechanisms in mitochondrial maintenance. *Curr. Biol.* **28**, R170–R185 (2018).
59. Sarraf, S. A. et al. Landscape of the PARKIN-dependent ubiquitylome in response to mitochondrial depolarization. *Nature* **496**, 372–376 (2013).
60. Shulga, Y. V., Topham, M. K. & Epand, R. M. Regulation and functions of diacylglycerol kinases. *Chem. Rev.* **111**, 6186–6208 (2011).
61. Yan, M. et al. Mitochondrial damage and activation of the cytosolic DNA sensor cGAS–STING pathway lead to cardiac pyroptosis and hypertrophy in diabetic cardiomyopathy mice. *Cell Death Discov.* **8**, 258 (2022).
62. Chen, Q., Sun, L. & Chen, Z. J. Regulation and function of the cGAS–STING pathway of cytosolic DNA sensing. *Nat. Immunol.* **17**, 1142–1149 (2016).
63. Leuschner, F. et al. Therapeutic siRNA silencing in inflammatory monocytes in mice. *Nat. Biotechnol.* **29**, 1005–1010 (2011).
64. Wang, J., Wei, L., Yang, X. & Zhong, J. Roles of growth differentiation factor 15 in atherosclerosis and coronary artery disease. *J. Am. Heart Assoc.* **8**, e012826 (2019).
65. Engel, K. M. et al. Reduced food intake and body weight in mice deficient for the G protein-coupled receptor GPR82. *PLoS One* **6**, e29400 (2011).
66. Chella Krishnan, K. et al. Sex-specific genetic regulation of adipose mitochondria and metabolic syndrome by Ndufv2. *Nat. Metab.* **3**, 1552–1568 (2021).
67. van Wetering, S. et al. VCAM-1-mediated Rac signaling controls endothelial cell-cell contacts and leukocyte transmigration. *Am. J. Physiol. Cell Physiol.* **285**, C343–C352 (2003).
68. Rotllan, N. et al. Hematopoietic Akt2 deficiency attenuates the progression of atherosclerosis. *FASEB J.* **29**, 597–610 (2015).
69. Sanchez-Lopez, E. et al. Choline uptake and metabolism modulate macrophage IL-1beta and IL-18 production. *Cell Metab.* **29**, 1350–1362.e1357 (2019).
70. Ray, B. K., Shakya, A., Turk, J. R., Apte, S. S. & Ray, A. Induction of the MMP-14 gene in macrophages of the atherosclerotic plaque: role of SAF-1 in the induction process. *Circ. Res* **95**, 1082–1090 (2004).

71. Chen, J. et al. Effect of M2 macrophage adoptive transfer on transcriptome profile of injured spinal cords in rats. *Exp. Biol. Med (Maywood)* **244**, 880–892 (2019).
72. Troiani, T. et al. Alternative macrophage polarisation associated with resistance to anti-PD1 blockade is possibly supported by the splicing of FKBP51 immunophilin in melanoma patients. *Br. J. Cancer* **122**, 1782–1790 (2020).
73. Pourcet, B. & Pineda-Torra, I. Transcriptional regulation of macrophage arginase 1 expression and its role in atherosclerosis. *Trends Cardiovasc Med.* **23**, 143–152 (2013).
74. Moore, K. J., Sheedy, F. J. & Fisher, E. A. Macrophages in atherosclerosis: a dynamic balance. *Nat. Rev. Immunol.* **13**, 709–721 (2013).
75. Robbins, C. S. et al. Local proliferation dominates lesional macrophage accumulation in atherosclerosis. *Nat. Med.* **19**, 1166–1172 (2013).
76. Wilson D. P. Is Atherosclerosis a Pediatric Disease? In: *Endotext* (eds et al.). MDText.com, Inc. Copyright © 2000-2022, MDText.com, Inc. (2000).
77. Moss, J. W. & Ramji, D. P. Cytokines: roles in atherosclerosis disease progression and potential therapeutic targets. *Future Med Chem.* **8**, 1317–1330 (2016).
78. Koelwyn, G. J., Corr, E. M., Erbay, E. & Moore, K. J. Regulation of macrophage immunometabolism in atherosclerosis. *Nat. Immunol.* **19**, 526–537 (2018).
79. Dutta, P. et al. Macrophages retain hematopoietic stem cells in the spleen via VCAM-1. *J. Exp. Med.* **212**, 497–512 (2015).
80. Cybulsky, M. I. et al. A major role for VCAM-1, but not ICAM-1, in early atherosclerosis. *J. Clin. Investig.* **107**, 1255–1262 (2001).
81. Mu, W., Chen, M., Gong, Z., Zheng, F. & Xing, Q. Expression of vascular cell adhesion molecule-1 in the aortic tissues of atherosclerotic patients and the associated clinical implications. *Exp. Ther. Med.* **10**, 423–428 (2015).
82. FOTIS, L. et al. Intercellular adhesion molecule (ICAM)-1 and vascular cell adhesion molecule (VCAM)-1 at the early stages of atherosclerosis in a rat model. *Vivo* **26**, 243–250 (2012).
83. Huang, L. S. et al. mtDNA activates cGAS signaling and suppresses the YAP-mediated endothelial cell proliferation program to promote inflammatory injury. *Immunity* **52**, 475–486.e475 (2020).
84. Nakayama, H. & Otsu, K. Mitochondrial DNA as an inflammatory mediator in cardiovascular diseases. *Biochem J.* **475**, 839–852 (2018).
85. Ballinger, S. W. et al. Mitochondrial integrity and function in atherogenesis. *Circulation* **106**, 544–549 (2002).
86. Guo, Y. et al. Mitochondrial DNA drives noncanonical inflammation activation via cGAS–STING signaling pathway in retinal microvascular endothelial cells. *Cell Commun. Signal.* **18**, 172 (2020).
87. Hu, M. et al. ATM inhibition enhances cancer immunotherapy by promoting mtDNA leakage and cGAS/STING activation. *J. Clin. Invest* **131**, e139333 (2021).
88. Willemsen, J. et al. TNF leads to mtDNA release and cGAS/STING-dependent interferon responses that support inflammatory arthritis. *Cell Rep.* **37**, 109977 (2021).
89. Yan, M. et al. Mitochondrial damage and activation of the cytosolic DNA sensor cGAS-STING pathway lead to cardiac pyroptosis and hypertrophy in diabetic cardiomyopathy mice. *Cell Death Discov.* **8**, 258 (2022).
90. Ishikawa, H., Ma, Z. & Barber, G. N. STING regulates intracellular DNA-mediated, type I interferon-dependent innate immunity. *Nature* **461**, 788–792 (2009).
91. Ablasser, A. et al. cGAS produces a 2′-5′-linked cyclic dinucleotide second messenger that activates STING. *Nature* **498**, 380–384 (2013).
92. Diner, E. J. et al. The innate immune DNA sensor cGAS produces a noncanonical cyclic dinucleotide that activates human STING. *Cell Rep.* **3**, 1355–1361 (2013).
93. Gao, P. et al. Cyclic [G(2′,5′)pA(3′,5′)p] is the metazoan second messenger produced by DNA-activated cyclic GMP-AMP synthase. *Cell* **153**, 1094–1107 (2013).
94. Zhang, X. et al. Cyclic GMP-AMP containing mixed phosphodiester linkages is an endogenous high-affinity ligand for STING. *Mol. Cell* **51**, 226–235 (2013).
95. Sun, L., Wu, J., Du, F., Chen, X. & Chen, Z. J. Cyclic GMP-AMP synthase is a cytosolic DNA sensor that activates the type I interferon pathway. *Science* **339**, 786–791 (2013).
96. Wu, J. et al. Cyclic GMP-AMP is an endogenous second messenger in innate immune signaling by cytosolic DNA. *Science* **339**, 826–830 (2013).
97. Wang, W. et al. STING promotes NLRP3 localization in ER and facilitates NLRP3 deubiquitination to activate the inflammasome upon HSV-1 infection. *PLoS Pathog.* **16**, e1008335 (2020).
98. Ning, L., Wei, W., Wenyang, J., Rui, X. & Qing, G. Cytosolic DNA-STING-NLRP3 axis is involved in murine acute lung injury induced by lipopolysaccharide. *Clin. Transl. Med* **10**, e228 (2020).
99. Gaidt, M. M. et al. The DNA inflammasome in human myeloid cells is initiated by a STING-cell death program upstream of NLRP3. *Cell* **171**, 1110–1124.e1118 (2017).
100. Ablasser, A. & Chen, Z. J. cGAS in action: expanding roles in immunity and inflammation. *Science* **363**, eaat8657 (2019).
101. Stumpf, J. D. & Copeland, W. C. Mitochondrial DNA replication and disease: insights from DNA polymerase γ mutations. *Cell Mol. Life Sci.* **68**, 219–233 (2011).
102. Zhong, Z. et al. New mitochondrial DNA synthesis enables NLRP3 inflammasome activation. *Nature* **560**, 198–203 (2018).
103. Xian, H. et al. Metformin inhibition of mitochondrial ATP and DNA synthesis abrogates NLRP3 inflammasome activation and pulmonary inflammation. *Immunity* **54**, 1463–1477.e1411 (2021).
104. Tigano, M., Vargas, D. C., Tremblay-Belzile, S., Fu, Y. & Sfeir, A. Nuclear sensing of breaks in mitochondrial DNA enhances immune surveillance. *Nature* **591**, 477–481 (2021).
105. Luft, R. & Landau, B. R. Mitochondrial medicine. *J. Intern Med.* **238**, 405–421 (1995).
106. Sorescu, D. & Griendling, K. K. Reactive oxygen species, mitochondria, and NAD(P)H oxidases in the development and progression of heart failure. *Congest Heart Fail* **8**, 132–140 (2002).
107. Jitschin, R. et al. Mitochondrial metabolism contributes to oxidative stress and reveals therapeutic targets in chronic lymphocytic leukemia. *Blood* **123**, 2663–2672 (2014).
108. Shigenaga, M. K., Hagen, T. M. & Ames, B. N. Oxidative damage and mitochondrial decay in aging. *Proc. Natl Acad. Sci. USA* **91**, 10771–10778 (1994).
109. Xian, H. et al. Oxidized DNA fragments exit mitochondria via mPTP- and VDAC-dependent channels to activate NLRP3 inflammasome and interferon signaling. *Immunity* **55**, 1370–1385.e1378 (2022).
110. Chen, Y. et al. Mitochondrial metabolic reprogramming by cd36 signaling drives macrophage inflammatory responses. *Circ. Res* **125**, 1087–1102 (2019).
111. Lavin, Y. et al. Tissue-resident macrophage enhancer landscapes are shaped by the local microenvironment. *Cell* **159**, 1312–1326 (2014).
112. Bisgaard, L. S. et al. Bone marrow-derived and peritoneal macrophages have different inflammatory response to oxLDL and M1/M2 marker expression - implications for atherosclerosis research. *Sci. Rep.* **6**, 35234 (2016).
113. Rios, F. J. et al. Oxidized LDL induces alternative macrophage phenotype through activation of CD36 and PAFR. *Mediators Inflamm.* **2013**, 198193 (2013).

114. Taketa, K. et al. Oxidized low density lipoprotein activates peroxisome proliferator-activated receptor-alpha (PPARalpha) and PPARgamma through MAPK-dependent COX-2 expression in macrophages. *J. Biol. Chem.* **283**, 9852–9862 (2008).
115. Nakae, J. et al. Novel repressor regulates insulin sensitivity through interaction with Foxo1. *EMBO J.* **31**, 2275–2295 (2012).
116. Yu, S. et al. Paneth cell-derived lysozyme defines the composition of mucolytic microbiota and the inflammatory tone of the intestine. *Immunity* **53**, 398–416.e398 (2020).
117. Ridker, P. M. How common is residual inflammatory risk? *Circ. Res.* **120**, 617–619 (2017).
118. Ference, B. A. et al. Mendelian randomization study of ACLY and cardiovascular disease. *N. Engl. J. Med.* **380**, 1033–1042 (2019).
119. Pinkosky, S. L., Groot, P. H. E., Lalwani, N. D. & Steinberg, G. R. Targeting ATP-citrate lyase in hyperlipidemia and metabolic disorders. *Trends Mol. Med.* **23**, 1047–1063 (2017).
120. Ouimet, M. et al. MicroRNA-33-dependent regulation of macrophage metabolism directs immune cell polarization in atherosclerosis. *J. Clin. Invest* **125**, 4334–4348 (2015).
121. Ouimet, M. et al. Mycobacterium tuberculosis induces the miR-33 locus to reprogram autophagy and host lipid metabolism. *Nat. Immunol.* **17**, 677–686 (2016).
122. Cimen, I. et al. Double bond configuration of palmitoleate is critical for atheroprotection. *Mol. Metab.* **28**, 58–72 (2019).
123. Venegas-Pino D. E., Banko N., Khan M. I., Shi Y. & Werstuck G. H. Quantitative analysis and characterization of atherosclerotic lesions in the murine aortic sinus. *J. Vis. Exp.* **82**, 50933 (2013).
124. Alves, T. C. et al. Integrated, Step-Wise, Mass-Isotopomeric Flux Analysis of the TCA Cycle. *Cell Metab.* **22**, 936–947 (2015).
125. Farr, A. G. et al. Medullary epithelial cell lines from murine thymus constitutively secrete IL-1 and hematopoietic growth factors and express class II antigens in response to recombinant interferon-gamma. *Cell Immunol.* **119**, 427–444 (1989).
126. Nguyen, Q. L. et al. Platelets from pulmonary hypertension patients show increased mitochondrial reserve capacity. *JCI Insight* **2**, e91415 (2017).
127. Brown, T. A. & Clayton, D. A. Release of replication termination controls mitochondrial DNA copy number after depletion with 2′,3′-dideoxycytidine. *Nucleic Acids Res.* **30**, 2004–2010 (2002).
128. Cable, D. M. et al. Robust decomposition of cell type mixtures in spatial transcriptomics. *Nat. Biotechnol.* **40**, 517–526 (2022).
129. Liao, Y., Wang, J., Jaehnig, E. J., Shi, Z. & Zhang, B. WebGestalt 2019: gene set analysis toolkit with revamped UIs and APIs. *Nucleic Acids Res* **47**, W199–W205 (2019).

Acknowledgements

This work was supported by National Institute of Health grants R00HL12076, R01HL143967, R01HL142629, R01 AG069399, and R01DK129339 to P.D.; the AHA Transformational Project Award (19TPA34910142), AHA Innovative Project Award (19IPLOI34760566) and ALA Innovation Project Award (IA-629694) to P.D.; the VMI Postdoctoral Training Program in Translational Research and Entrepreneurship in Pulmonary and Vascular Biology T32 funded by the National, Heart, Lung and Blood Institute (NHLBI) and United Therapeutics Jenesis award to J.F; and NHLBI F32HL146000 to N.N. cDNA generation, library preparation, and sequencing were performed by the University of Pittsburgh Health Science Sequencing Core at the UPMC Children's Hospital of Pittsburgh, Pittsburgh, PA, USA. We thank the NIH-supported microscopy resources at the Center for Biologic Imaging (NIH grant 1S10OD019973-01). We thank the NIH-supported FACS resources at the Unified Flow Core (NIH grant 1S10OD032265). Figure panels 1A, E, 6B, 6F were created with BioRender.com, released under a Creative Commons Attribution-NonCommercial-NoDerivs 4.0 International license.

Author contributions

J.F. and N.N. conducted experiments, analyzed the data, and wrote the paper. L.L., L.O., E.J., J.S., Ya.Z., A.R.J., K.R., and X.L. conducted experiments. S.P.O conducted experiments and analyzed the data. S.S. assisted with metabolomics analysis. Yi.Z., S.T., and S.S. reviewed the manuscript. J.D. and H.X. performed the spatial single-cell transcriptomics analysis. P.D. designed the research study, analyzed the data, and composed the manuscript.

Competing interests

The authors declare no competing interests.

Additional information

Supplementary information The online version contains supplementary material available at https://doi.org/10.1038/s41467-024-51780-1.

Correspondence and requests for materials should be addressed to Partha Dutta.

Peer review information *Nature Communications* thanks Esther Lutgens and the other, anonymous, reviewer(s) for their contribution to the peer review of this work. A peer review file is available.